The Thesis Committee for Ryan Wai-Hung Leung
Certifies that this is the approved version of the following Thesis:

Development of a Hydrate-Gas-Water Static Equilibrium Model and Analysis of Three-Phase Stability

APPROVED BY
SUPERVISING COMMITTEE:

Hugh Daigle, Supervisor

David A. DiCarlo

Development of a Hydrate-Gas-Water Static Equilibrium Model and Analysis of Three-Phase Stability

by

Ryan Wai-Hung Leung

Thesis

Presented to the Faculty of the Graduate School of

The University of Texas at Austin

in Partial Fulfillment

of the Requirements

for the Degree of

Master of Science in Engineering

The University of Texas at Austin

May 2018

To my Creator, my Lord and Savior, and my Holy Companion

Acknowledgements

I first want to thank my advisor, Dr. Hugh Daigle. Since the beginning when I first started working with him as a junior undergraduate student, I have grown so much as a researcher and engineer under his guidance. I am grateful for the countless times he steered me in the right direction and gave me insight into the realm of gas hydrates and geophysics. I deeply appreciate the opportunity Hugh gave me to go to ICGH9, GRS, and GRC. My work is funded under project DE-FE0013919, and I also show great gratitude to the Department of Energy for making this all possible.

I thank Dr. David DiCarlo for being my second reader and for the discussions on three-phase stability. I am also thankful for the many conversations with Michael Nole, Abhishek Bihani, Zach Murphy, and all of the UT Hydrates friends from the Jackson School. I want to give a big shout-out to Dr. Nicolas Espinoza, since he was the one who first introduced me to the gas hydrates research at UT Austin.

I thank all of my officemates, past and present, for all of the interesting conversations we've had. Brian Lee, my neighbor, brought me new perspectives almost every day. Also, I have much appreciation for Brandon Tang and Denning Wang for supporting me and sticking with me through our six years at UT PGE. I thank UT PGE for all the opportunities and knowledge I've gained during my time as an undergraduate and graduate student.

Of course, I wouldn't be here writing this without the endless support from my family. Mom and Dad, I thank you for always being there for me.

Finally, I thank my Lord and Maker Jesus Christ, to whom this is dedicated to, for giving me the strength, intelligence, endurance, and willpower to finish this work.

Abstract

Development of a Hydrate-Gas-Water Static Equilibrium Model and Analysis of Three-Phase Stability

Ryan Wai-Hung Leung, M.S.E.

The University of Texas at Austin, 2018

Supervisor: Hugh Daigle

Recent evidence suggests that a three-phase stability zone exists at the base of gas hydrate stability (BGHS), where hydrate and gas may coexist due to the pore size distribution. We develop a three-phase stability zone model at static equilibrium based on the idea of minimizing interfacial energy. We use this model to produce three-phase saturations and study the effects of three-phase stability for two applications.

The first application is related to the migration of gas from beneath sealing hydrate layers to the seafloor. A proposed mechanism for this upwards gas migration is the generation of fractures through the sealing hydrate sediment due to overpressures caused by the accumulation of gas on geologic timescales. Our study focuses on how the fracturing potential of a three-phase stability zone differs from a discrete BGHS, where hydrate is separated from gas by a sharp boundary. We model gas overpressures at Blake Ridge, Hydrate Ridge, and the Kumano Basin by incorporating mercury intrusion capillary pressure data with our three-phase stability model. Our results show that the overpressures in the three-phase stability model are smaller, reducing the potential for

gas-driven fracturing. We also find that hydrate-bearing basins with shallower seafloor depths modeled with three-phase stability need much more methane to generate the overpressures that will initiate fractures.

The second application of three-phase stability relates to the bottom-simulating reflection (BSR), which is a common negative polarity reflection in marine sediments that often follows the contour of the seafloor. Recent literature suggests that the BSR indicates the shallowest presence of gas, not the BGHS. This three-phase stability model has an impact on the seismic response of the BSR, and we study this effect by developing 1-D rock physics models of Blake Ridge. By varying the methane quantity and performing fluid substitution with three-phase saturation profiles, we generate synthetic seismograms and analyze the difference in two way travel time (TWTT). For comparison, we use the workflow for a parameter sensitivity model and an original-resolution model. Through this analysis, we find a relationship between the TWTT width of the BSR's peaks and the methane abundance at the BGHS.

Table of Contents

List of Tables

List of Figures

Chapter 1: Introduction

1.1 Overview of Methane Hydrates

Under a range of temperature, pressure, and salinity conditions, methane and water can form stable ice-like crystalline compounds called methane hydrate. The formation of methane hydrates naturally occurs in shallow depths of permafrost regions and in the uppermost few hundred meters of sediments beneath the seafloor on continental margins where pressures are higher and temperatures are lower. There is a large body of research focusing on naturally occurring hydrates because of their potential as a subsurface geohazard (Dillon et al., 1998; Kvenvolden, 1993), a climate change influencer (Archer and Buffett, 2005; Dickens et al., 1997a), and an energy resource (Boswell, 2009; Collett, 1992). Significantly affecting these aspects of hydrates is their spatial distribution within the subsurface. The formation of methane hydrate requires a natural supply of methane, which can be formed microbially or thermogenically; methane migration, through multiple transport processes, can lead to the formation of methane hydrates within sediments found in the hydrate phase stability envelope. Overall, the study of methane hydrates is very broad, and we encourage curious readers to learn of the other various aspects of methane hydrates not covered in this work.

We emphasize here a note to the reader: a more general term describing methane hydrates is natural gas hydrates. Other natural gases like ethane can also form hydrate in the right pressure and temperature conditions. However, methane is the dominant natural gas that forms hydrate in our studies. Other chemical elements or compounds can also form hydrates, like carbon dioxide, nitrogen, and xenon, but these types of hydrates are not the focus of this work. While methane hydrate is the appropriate term describing the substance this work focuses on, we will use more clarifying words from here on. We

refer to hydrate as the solid phase, gas as the gaseous phase, and water as the aqueous phase. Additionally, methane will be used to indicate the chemical component CH_4, usually in terms of mass.

1.2 Research Objectives

The main goal of this thesis is to investigate the three-phase stability zone, where the hydrate, gas, and water phase coexist. We will analyze two applications that study the effect of three-phase stability. To carry this out, this research performs the following:

1. Develop a static equilibrium model that can solve for three-phase stability given temperature and pressure conditions
2. Investigate how three-phase stability affects gas overpressure caused by gas buildup beneath hydrate-bearing sediments and how the overpressure influences fracture initiation
3. Generate synthetic seismograms for the three-phase stability zone to simulate and analyze a more realistic seismic response at the bottom simulating reflection

1.3 Outline

Chapter 1 serves as the introduction to our research topic and objectives.

Chapter 2 reviews the literature of three-phase stability, along with describing previous work and methodology pertaining to gas overpressure beneath hydrate-bearing sediments and the study of the bottom simulating reflection.

Chapter 3 details the development of the three-phase stability model, which generates phase saturation profiles for hydrate, gas, and water under static equilibrium conditions. This chapter also covers the 1-D rock physics model used to generate synthetic seismograms for different fluid profiles at the bottom simulating reflection.

Chapter 4 covers the effect of three-phase stability on gas overpressure which can lead to fracture initiation. We discuss how gas overpressure differs in the three-phase stability case from a simpler three-phase bulk equilibrium case where a hydrate layer with no gas overlays a gas layer with no hydrate. We perform this analysis for three offshore locations and use data from multiple scientific expeditions to see how overpressure-induced fracture initiation is influenced by the hydrate-bearing sediment properties.

Chapter 5 contains the analysis of bottom simulating reflections when taking three-phase stability into account. We use well log data from a scientific drilling expedition to build a 1-D rock physics model, and we see how phase saturation gradients within a transition zone (stability zone) influence the seismic response. We also look at some quantitative trends of how the effect of the three-phase stability zone changes when more methane is added into the system.

Chapter 6 concludes this research by summarizing key findings and presenting suggestions for future work.

Chapter 2: Literature Review

2.1 Three-Phase Stability

In sedimentary rock layers underneath the seafloor, methane can exist in multiple phases, depending on the pressure and temperature condition and the water salinity. A small but non-negligible concentration of methane can be dissolved in the water phase. Methane can also form a hydrate or gas phase; hydrate naturally forms in shallower depths, and gas is stable in deeper depths, both due to sediment pressure and temperature gradients. If we assume that our methane system can be imagined as an open container, then the hydrate and gas phases will form under bulk conditions. For constant pressure and temperature gradients, bulk conditions will force the hydrate and gas phase to segregate by depth, since methane will be more stable in one phase over the other for a given depth. Under bulk conditions, there exists a single depth where hydrate and gas can coexist; this is the depth of three-phase bulk equilibrium.

If we relax the bulk condition assumption, we will have to account for capillary effects since the different phases will reside in pores with a given pore size. Capillary effects influence hydrate phase stability in porous media; this effect has been measured experimentally (Anderson et al., 2003, 2009; Handa and Stupin, 1992; Østergaard et al., 2002; Uchida et al., 1999, 2004) and modeled theoretically (Clennell et al., 1999; Henry et al., 1999; Liu and Flemings, 2011; Smith et al., 2002; Sun and Duan, 2007). However, accounting for capillary effects assuming a single, constant pore size will not dramatically change the phase stability of the methane system; a constant capillary effect will allow hydrate and gas to coexist only at the depth of three-phase "capillary-adjusted" bulk equilibrium.

To achieve three-phase stability of hydrate, gas, and water over a range of depths, our porous media needs to have a distribution of pore sizes instead of only one pore size. Marine sediments can have a wide range of pore sizes in sands and clays, leading to porous media with narrow or broad pore size distributions. Some studies have investigated capillary effects on both the hydrate and gas phase when there is a distribution of pore sizes (Clennell et al., 1999; Henry et al., 1999; Liu and Flemings, 2011). Three-phase stability is related to the supersaturation of methane dissolved in water; capillary effects increase the amount of interfacial energy required to form a curved hydrate or gas phase within a pore, and this increase in energy is matched with an increase in supersaturation of the water phase. Therefore, since hydrate and gas can form in a range of pore sizes due to varying responses to capillary effects, three-phase stability can be achieved with different phases occupying different pore sizes (Clennell et al., 1999; Henry et al., 1999).

2.1.1 Capillary Effects

Capillary pressure is the pressure difference across a curved interface between two phases. This pressure difference is a function of the curvature of the interface and the interfacial tension between the two phases. When this interface resides inside a pore, the pore radius and the wettability of the solid grain surface both affect the curvature of the interface, which changes the capillary pressure. Wettability is normally represented by the contact angle formed between the two-phase contact surface and the solid grain surface. Wetting phases have smaller contact angles (<90°) with the surface, and non-wetting phases have larger contact angles (>90°) with the surface.

The Washburn equation relates the capillary pressure caused by an interface between two phases in a cylindrical pore to the contact angle θ, interfacial tension σ, and

pore radius r. The Washburn equation for the capillary pressure P_c across a hydrate-water interface and a gas-water interface is

$$P_{c,gw} = -\frac{2\sigma_{gw}\cos\theta_{gw}}{r_g} \tag{2.1}$$

$$P_{c,hw} = -\frac{2\sigma_{hw}\cos\theta_{hw}}{r_h} \tag{2.2}$$

where the subscripts gw and hw indicate either gas-water or hydrate-water interfaces. When there is a distribution of pore sizes, r_g is the radius of the smallest pore saturated with the gas phase, and r_h is the radius of the smallest pore saturated with the hydrate phase. For modeling purposes, we use $\sigma_{gw} = 0.072$ J/m^2 and $\sigma_{hw} = 0.027$ J/m^2 (Clennell et al., 1999; Henry et al., 1999).

Mercury intrusion capillary pressure (MICP) experiments inject mercury into an air-saturated rock core sample, replicating a capillary drainage process. During the experiment, the mercury injection pressure is measured, which is the mercury-air capillary pressure. After a MICP experiment is done on a particular rock sample, we can convert the mercury-air capillary pressure to gas-water or hydrate-water capillary pressure using the interfacial tensions and contact angles for each respective interface. By assuming that the pore network is well-connected and that the non-wetting phase telescopically invades the pores starting with the largest pores first, we can use the converted capillary pressure curves as a substitute for a quantified pore size distribution. Thus, we have a direct relation from a given non-wetting saturation, or the injected volume normalized by the pore volume of the sample, to the corresponding capillary pressure of the non-wetting phase.

For a two-phase system, the actual capillary pressure calculation is straightforward; empirical models like the Brooks-Corey or Van Genuchten model can be

fitted to MICP data, and these models can then analytically calculate capillary pressure for a given non-wetting saturation (Brooks and Corey, 1964; Van Genuchten, 1980). Alternatively, capillary pressures can be interpolated from the MICP data itself for any non-wetting saturation.

2.1.2 Methane Solubility

We need to know the bulk methane solubilities for two separate systems to calculate the distribution of hydrate and gas phase saturations. The first system is a gas-water system where all the mass of methane either forms the gas phase or dissolves in the water phase. The second system is a hydrate-water system where all the methane forms a hydrate phase or dissolves in water. For both these systems, the formation of a non-wetting phase requires that the water phase be supersaturated with methane, so that any addition of methane mass will form the corresponding second phase. Both of the bulk methane solubilities can be calculated as a function of temperature, pressure, and water salinity using two different equations of state (EOS). We calculate the bulk methane solubility for a hydrate-water system using the method of Davie et al. (2004), and we use the EOS from Duan et al. (1992) to calculate the bulk methane solubility for a gas-water system. Both of these EOS are fairly complex, so we refer the reader to the literature. We also note that these EOS are by no means the only EOS available to calculate the bulk methane solubility for a gas-water and hydrate-water system; alternative or more recent models include Henry et al. (1999) and Duan et al. (2011).

By assuming that the pressure gradient, temperature gradient, and salinity are constant, we can calculate smooth and continuous bulk methane solubility curves as a function of depth. Generally, solubility decreases with depth for a hydrate-water system, and solubility increases with depth for a gas-water system (Liu and Flemings, 2011). The

intersection of the two bulk solubility curves gives the depth of three-phase bulk equilibrium.

For a two-phase hydrate-water system, the Gibbs-Thomson effect causes the methane solubility to increase when the hydrate phase occupies pores instead of being in bulk (Clennell et al., 1999; Henry et al., 1999). We use the Gibbs-Thomson equation to calculate the dimensionless increase in methane solubility (ΔC_{H-W}) caused by the solid-liquid interface increasing the Gibbs free energy (Clennell et al., 1999):

$$\Delta C_{H-W} = \frac{\Delta\mu}{RT} = P_{c,hw}\frac{nV_\beta}{RT} \tag{2.3}$$

where n is the hydrate stoichiometry factor ($n = 5.75$ for structure I methane hydrate), V_β is the molar volume of the water within the hydrate lattice ($V_\beta = 22.6$ cm^3/mol from Henry et al. (1999)), R is the universal gas constant, and T is the absolute temperature.

Likewise, for a two-phase gas-water system, the methane solubility in a pore increases due to Henry's law. Since the partial pressure of the gas is proportional to the gas capillary pressure, we can approximate the dimensionless increase in methane solubility (ΔC_{G-W}) using $P_{c,gw}$:

$$\Delta C_{G-W} = \frac{P_{c,gw}}{P_w} \tag{2.4}$$

where P_w is the hydrostatic water pressure. We finally calculate the system methane solubilities (C_{H-W} for hydrate-water, C_{G-W} for gas-water), which are elevated due to capillary effects, by scaling the bulk solubilities with the dimensionless increase:

$$C_{H-W} = (1 + \Delta C_{H-W})C_{H-W}^{Bulk}(P,T) \tag{2.5}$$

$$C_{G-W} = (1 + \Delta C_{G-W})C_{G-W}^{Bulk}(P,T) \tag{2.6}$$

2.1.3 Pore Models Developed in the Past

Liu and Flemings (2011) theorized a pore model that can achieve three-phase stability. There are several pore model assumptions that are necessary for a three-phase stability model, and we summarize these key assumptions from the literature below. Pores are assumed to be cylindrical in shape and connected through narrow pore throats. The cylindrical pores have a distribution of pore radii that can be inferred through MICP data. The wettability of the pore walls are completely water wet, so the contact angle between water and the pore wall is 0 degrees. This allows water to form a continuous film that connects all of the pores and completely saturate all of the pore throats. Hydrate and gas are both completely non-wetting, so both of the non-wetting phases occupy the cylindrical pore bodies without contacting the pore wall. Since we assume both hydrate and gas are completely non-wetting, we set $\theta_{gw} = \theta_{hw} = 180°$. The capillary pressure of the non-wetting phase can be calculated from the smallest pore radius of the pore that the non-wetting phase resides in.

The difficulty in achieving three-phase stability arises when we attempt to calculate three-phase capillary pressures. The Washburn equation is for two-phase capillary pressure, so an assumption on how three phases will occupy the pore space has to be made. The pore occupancy assumption in Liu and Flemings (2011) is a 50%-50% split where both the hydrate and gas phases can occupy the same pore size in equally. Given the phase saturations S_h and S_g, Liu and Flemings (2011) calculates the capillary pressures by first determining which non-wetting phase has a greater saturation. Since both phases fill the pore space starting with the largest pores first, both phases will occupy the large pores together. The phase with more saturation will be able to reach a smaller pore size than the other phase, and will occupy 100% of the pore space from then

on. Therefore, the capillary pressure of the phase with greater saturation can be found by using an "effective saturation" for the two-phase capillary pressure function:

$$P_{c,nw}^{3P} = P_{c,nw}^{2P}\left(S_g + S_h\right) = P_{c,nw}^{2P}(1 - S_w) \tag{2.7}$$

where $P_{c,nw}^{3P}$ is the three-phase capillary pressure of either non-wetting phase, $P_{c,nw}^{2P}$ is the two-phase capillary pressure formula of that same non-wetting phase. For the other non-wetting phase with less saturation, the capillary pressure is found by using a different "effective saturation" with the two-phase capillary pressure function:

$$P_{c,nw}^{3P} = P_{c,nw}^{2P}(2S_{nw}) \tag{2.8}$$

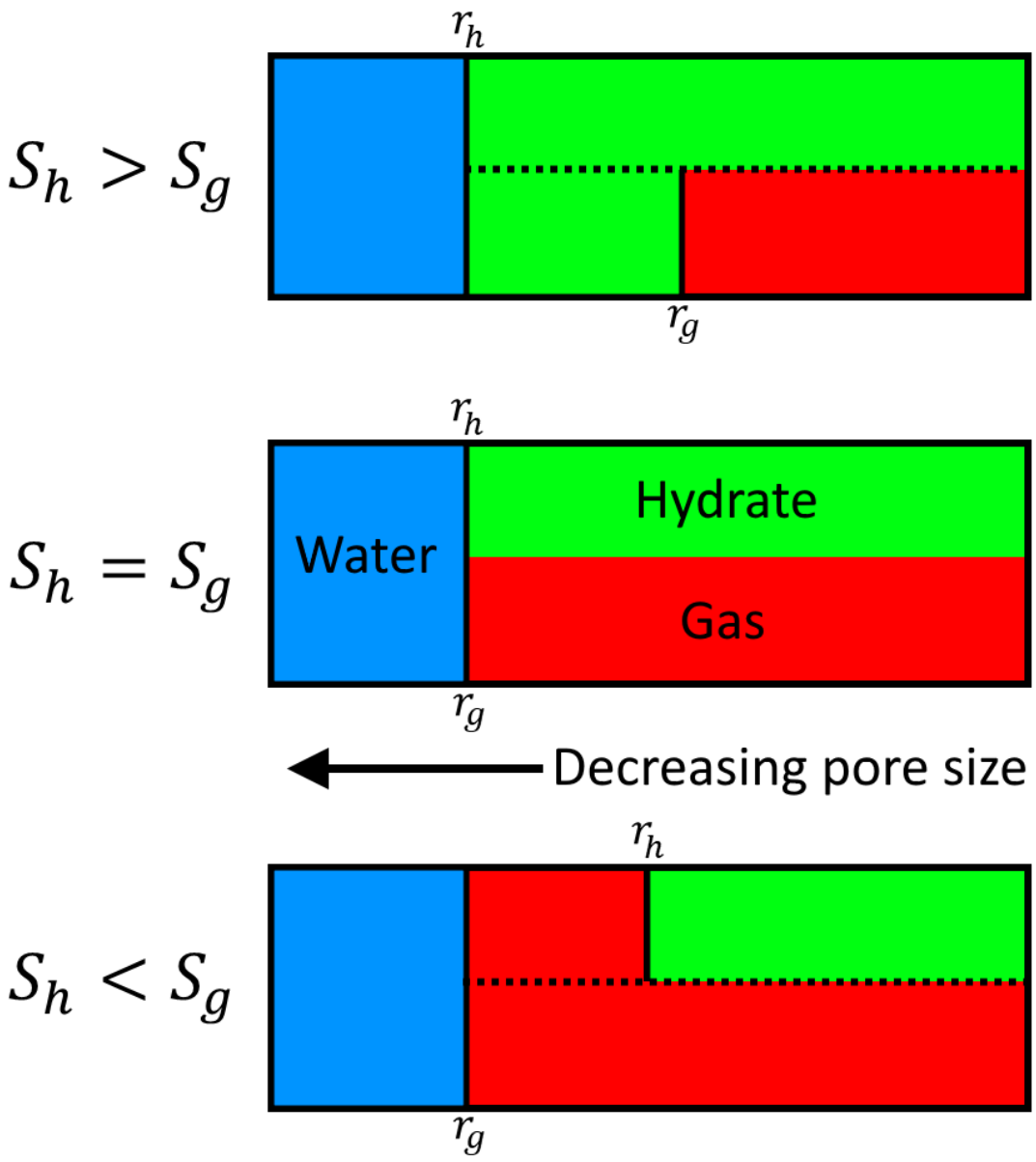
r_h
$S_h > S_g$
r_g
r_h
$S_h = S_g$
Water
Hydrate
Gas
r_g
Decreasing pore size
r_h
$S_h < S_g$
r_g

Figure 2.1

Figure 2.1 Schematic showing the 50%-50% pore occupancy model graphically. Assuming we are given S_h and S_g, we consider two cases: either $S_h > S_g$ or $S_h < S_g$. If $S_h > S_g$, then hydrate fills down to the pore size r_h shown in the top diagram. In order to reach r_h and achieve the associated capillary pressure for an equivalent two-phase hydrate-water system, all of the S_g will have to act like S_h, so for the three-phase case, the hydrate capillary pressure will be proportional to $S_h + S_g$. Likewise, for S_g to reach r_g, the gas would have to double its saturation in a gas-water case; therefore the gas capillary pressure will be proportional to $2S_g$. If $S_h < S_g$, then the same mechanics apply; the phases will only be switched from the example above. In the rare case that $S_h = S_g$, the two formulas for calculating the effective saturation become the same.

Using this formulation, Liu and Flemings (2011) were able to converge on a solution when solving for three-phase stability. This allows the calculated capillary pressures of both phases to be continuous over all depths, including when the methane system changes between two-phase and three-phase at the top and bottom of the stability zone.

2.2 Gas Overpressure in Hydrate-Bearing Sediments

As a solid phase, hydrates can clog up sediment pore space, reducing permeability and effectively causing upward-migrating gas to accumulate beneath a sealing hydrate layer. The buildup of gas underneath the hydrate stability zone on geological timescales can critically pressurize the gas (Flemings et al., 2003; Jain and Juanes, 2009), to the point where the overpressure begins to fracture the sediment and create small conduits that allow upward migration. The overpressure-induced fractures themselves can extend upwards, continuing until a high permeability channel to the seafloor is eventually formed. Other work has shown how overpressure due to gas buildup can cause faults to slip within hydrate-saturated sediments; this can create gas chimneys which allow gas to quickly migrate from below a hydrate layer to the bottom of the ocean (Hornbach et al., 2004). Advective gas flux can also cause hydraulic fractures in fine-grained sediment as hydrate blocks the pores (Daigle and Dugan, 2011). Understanding the fracturing behavior associated with hydrates and the related gas migration through fractures is essential for understanding hydrate-associated methane release from the seafloor.

2.2.1 Fracture Criterion

To investigate fractures initiating through gas overpressure, we use the fracture criterion from past literature. It has been shown when the pore pressure exceeds the

minimum horizontal stress of a fluid-filled porous rock, hydraulic (tensile) fractures will initiate (Valkó and Economides, 1995). From poroelasticity theory, we can estimate the minimum horizontal stress ($\sigma_{h,min}$) of the porous rock from the overburden (σ_{vh}), which is normally assumed to be the maximum principal stress:

$$\sigma_{h,min} = \left(\frac{\nu}{1-\nu}\right)\left(\sigma_{vh} - \alpha P_p\right) + \alpha P_p \tag{2.9}$$

where, α is Biot's constant, ν is Poisson's ratio, and P_p is the pore pressure. We set $\alpha = 1$, since shallow marine sediments are naturally unconsolidated; the porosity of unconsolidated sediments is relatively high, so Biot's constant is close to unity. Poisson's ratio is taken as 0.4, which is also common for unconsolidated sediments (Karig and Hou, 1992; Reynolds, 1997). We subtract the pore pressure from the stresses to obtain the effective stresses:

$$\sigma'_{h,min} = \left(\frac{\nu}{1-\nu}\right)\left(\sigma'_{vh}\right) \tag{2.10}$$

We define the overpressure ratio as the ratio of the pore pressure that is in excess of hydrostatic pressure (P^*) to the vertical effective stress under hydrostatic conditions. Gas overpressure can be used as P^*, so when P^* becomes equal to the minimum horizontal effective stress, a fracture can be initiated. By substituting the definition of $\sigma'_{h,min}$ for P^*, we obtain the commonly defined fracture criterion

$$\lambda^* = \frac{P^*}{\sigma'_{vh}} = \frac{\nu}{1-\nu} \tag{2.11}$$

where $\lambda^* = 0.67$ for $\nu = 0.4$ (Daigle and Dugan, 2011). By assuming the water phase is hydrostatically pressured, the gas capillary pressure is equivalent to gas overpressure P^*, since the gas capillary pressure is the differential pressure between the gas and hydrostatically pressured water phase.

2.3 Bottom Simulating Reflection and Previous Interpretations

For over half a century, bottom simulating reflections (BSRs) have been identified and studied within the geophysical literature. A BSR is routinely interpreted from seismic traces as an acoustic reflection that runs subparallel to the seafloor with an opposite polarity compared to the seismic reflection at the seafloor (Kvenvolden and Barnard, 1983). Physically, this occurs because the BSR originates from a strong negative acoustic impedance contrast when the seismic wave transitions from a higher-density, faster-velocity sediment layer to a lower-density, slower-velocity layer. This common phenomenon has been used as evidence of the existence of hydrate-bearing sediments above the BSR and gas bearing sediments existing below the BSR (Kvenvolden and Barnard, 1983).

Much of the early research focusing on BSRs found across the world concluded that the BSR is located at the base of gas hydrate stability (BGHS), which is the deepest depth where hydrate can exist within the phase envelope defined by local pressure, temperature, and pore water salinity (Bryan, 1974; Shipley et al., 1979; Tucholke et al., 1977). However, recent studies suggested that the BSR instead indicates the shallowest presence of gas, since a small amount of gas saturation can cause large impedance shifts. Therefore, the BSR may not be necessarily collocated with the BGHS. With this theory, the BSR marks the gas phase upper boundary, so the BGHS can possibly be located beneath the BSR. With this view, the BSR and BGHS both frame the three-phase stability zone, since the top of the three-phase zone is marked by the shallowest occurrence of gas, and the bottom is set by the deepest occurrence of hydrate (Hillman et al., 2017; Liu and Flemings, 2011).

Chapter 3: Modeling

3.1 Phase Saturation Models

In this section, we develop the three-phase stability model that can solve for the coexistence of hydrate, gas, and water phases. Additionally, we also construct a simple two-phase model for comparison with the three-phase stability model. This model generates hydrate-water system saturations above the depth of three-phase bulk equilibrium and generates gas-water system saturations below that same depth. Since the depth of three-phase bulk equilibrium separates both two-phase systems, we coin this model the three-phase bulk equilibrium model.

We build off of the workflow established in Liu and Flemings (2011), which is covered in section 2.1. The rest of this section introduction covers other necessary model assumptions. This work focuses on a geological timescale, so we assume equilibrium and static conditions, so there are no kinetics and transport. We set the water phase pressure to its hydrostatic pressure. For all depths, the sediment is assumed to have the same pore size distribution. As mentioned before, we consider methane as the only mass component in addition to water; the hydrate and water phase are comprised of methane and water, while the gas phase is made up entirely of methane.

We use mass balance equations for both the three-phase bulk equilibrium model and the three-phase stability model, and these equations are normalized by the pore volume to utilize saturation terms. Because of this, our total methane mass term is also normalized to the pore volume; the mass term is coined the methane quantity, which has units of kilogram methane per cubic meter of pore volume. The methane quantity represents the density of methane in the pore space and is a model parameter that we set and adjust in both phase saturation models. For simplicity, we usually assume a constant

methane quantity for all depths of the system. However, the phase saturations are strictly only a function of pressure, temperature, salinity, and methane quantity, so the model uses the same algorithm whether the methane quantity is constant across all depths or the methane quantity has gradients. It is also possible to set the system's methane solubility and solve for the saturations and methane quantity. This methodology can be used to see the effects of different methane solubility profiles in depth. Future work can explore these possibilities.

3.1.1 Three-Phase Bulk Equilibrium Model

Our three-phase bulk equilibrium model conceptually represents an accumulation of gas beneath a hydrate layer at static equilibrium with no capillary effects. We model this representation as a two-phase system stacked with two layers; these layers are separated at the depth of three-phase bulk equilibrium (z_{3P}^{Bulk}). The intersection of the gas-water and hydrate-water bulk methane solubility curves determines the z_{3P}^{Bulk}. Above the z_{3P}^{Bulk}, only hydrate coexists with supersaturated water. Below the z_{3P}^{Bulk}, only gas coexists with supersaturated water. Since C_{H-W}^{Bulk} increases with depth and C_{G-W}^{Bulk} decreases with depth, the two solubility curves intersect a few hundred meters below the seafloor for common pressure and temperature gradients.

Above the z_{3P}^{Bulk}, we use a mass balance on methane to determine how much methane mass forms the hydrate phase and how much methane dissolves into the water phase. If not enough methane concentration is available to supersaturate the water, the hydrate phase does not have a chance to form. The following equations are used to solve for the water (S_w) and hydrate (S_h) saturations:

$$S_w \rho_w C_{CH_4} + S_h \rho_h f_{CH_4} = M_{CH_4} \tag{3.1}$$

$$S_w + S_h = 1 \tag{3.2}$$

$$C_{CH_4} = C_{H-W}^{Bulk}(P,T) \tag{3.3}$$

where M_{CH_4} is a given methane quantity, C_{CH_4} is the methane solubility of the continuous water phase, ρ_w is the water density, ρ_h is the hydrate density, and f_{CH_4} is the mass fraction of methane in a hydrate cage ($f_{CH_4} = 0.1341$ for structure I methane hydrate). The density of water is taken to be 1.024 g/cm^3, and the density of hydrate is taken to be 0.924 g/cm^3 (Helgerud et al., 2009). Since we assume the system is at bulk equilibrium with no capillary effects, the system's methane solubility is equal to the $C_{H-W}^{Bulk}(P,T)$ found using Davie et al. (2004).

Below the z_{3P}^{Bulk}, methane mass balance is used to solve for the gas (S_g) and water saturations in the gas layer. As with the hydrate layer, a supersaturation of the water phase is required before the gas phase can form.

$$S_w \rho_w C_{CH_4} + S_g \rho_g = M_{CH_4} \tag{3.4}$$

$$S_w + S_g = 1 \tag{3.5}$$

$$C_{CH_4} = C_{G-W}^{Bulk}(P,T) \tag{3.6}$$

We use the ideal gas law to determine ρ_g, the density of gas. This was done to best align our modeling results with geophysical observations (Liu and Flemings, 2011). The methane solubility C_{CH_4} equals the $C_{G-W}^{Bulk}(P,T)$ calculated using the EOS from Duan et al. (1992).

3.1.2 Three-Phase Stability Model

Our three-phase stability model follows a similar workflow to the three-phase bulk equilibrium model, but we now include capillary effects. Our main contribution to modeling three-phase stability comes from successfully implementing a different pore occupancy assumption. In contrast to the 50%-50% pore occupancy assumption proposed in Liu and Flemings (2011), we base our new pore occupancy assumption on the minimization of interfacial energy. For any given physical pore, we assume that only one non-wetting phase, either hydrate or gas, will occupy the pore body. Additionally, the continuous water film is still covering the pore walls.

Theoretically, if hydrate, gas, and water coexist within the same physical pore, the force balance on the phase interfaces yields $\sigma_{hg} = \sigma_{hw} + \sigma_{gw}$ with the contact angles we assume earlier (Clennell et al., 1999). Since the hydrate-gas interface requires the highest interfacial energy (σ_{hg}), individual hydrate and gas phases will tend to occupy different pores in order to minimize the total interfacial energy. As a result, the segregation of the hydrate phase and the gas phase within individual pores allows us to describe the capillary effects of a three-phase system by combining the effects of both two-phase systems.

Since the energy required for creating gas-water interfacial area is greater than the energy required for creating hydrate-water interfacial area, we assume that the gas phase fills the largest pore sizes and the hydrate fills the smaller pore sizes, with water filling the remaining smallest pore sizes. This configuration theoretically minimizes the total interfacial energy of the system. The interfacial energy minimization theory forces our model to converge to a new solution for three-phase stability while still fulfilling the continuous capillary pressure condition.

Figure 3.1

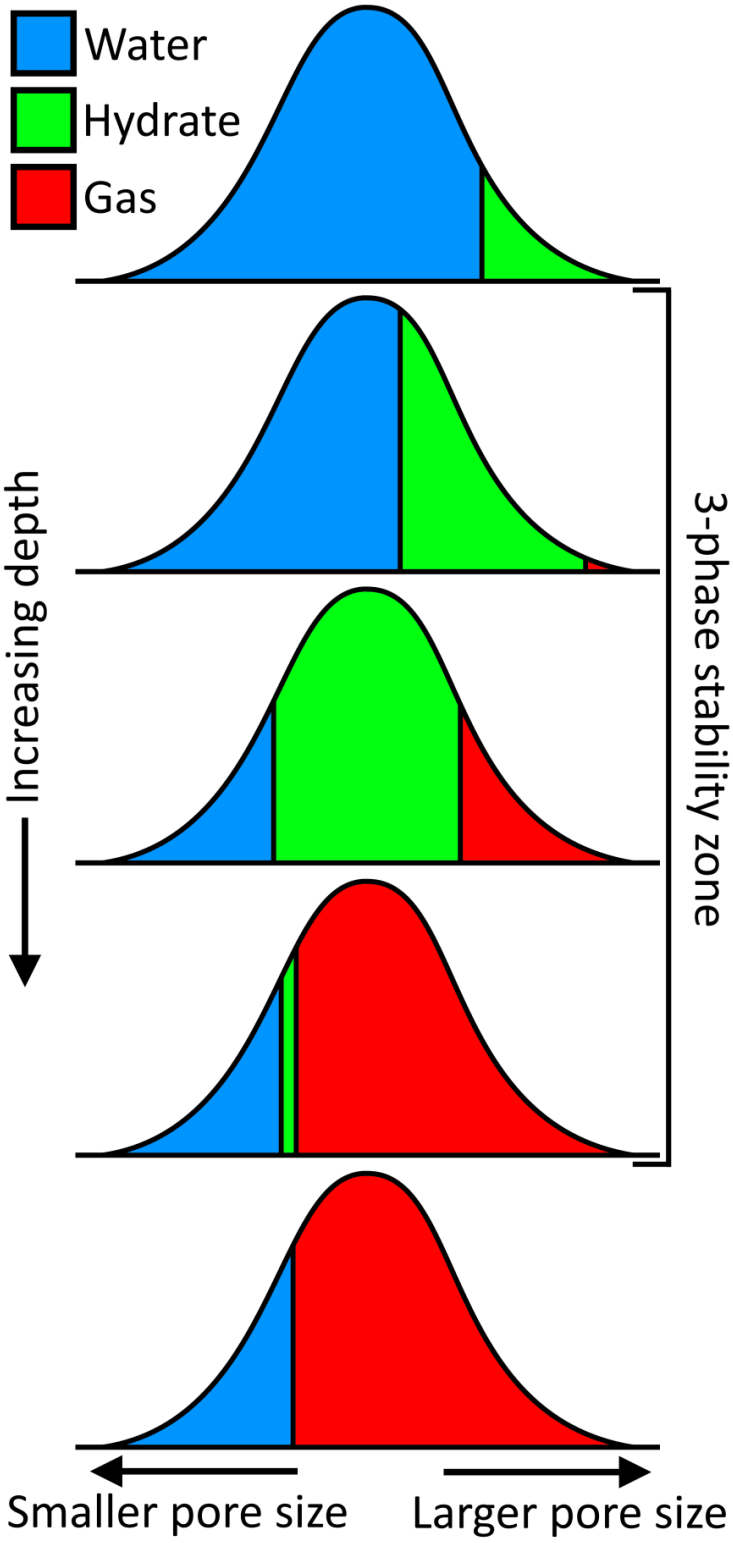
Water
Hydrate
Gas
Increasing depth
3-phase stability zone
Smaller pore size
Larger pore size

Figure 3.1 Schematic of the sequence of phase saturation distributions within a distribution of pore sizes. Each diagram represents the segregation of the hydrate, gas, and water phase for a given pore size distribution in or around the depths of three-phase stability. Above the three-phase zone, all the methane dissolves into water or forms hydrate. Hydrate occupies the largest pore sizes since it is the non-wetting phase. Just below the top of the three-phase zone, the gas phase becomes stable. Because of the minimization of interfacial energy, gas fills the largest pore size while hydrate moves into smaller pore sizes. This continues deeper into the three-phase zone. Near the bottom of three-phase stability, the remaining hydrate saturation is pushed into the smallest pores, and gas occupies all the pores larger than the pore size the hydrate resides in. Once past the bottom of the three-phase zone, hydrate no longer can form, and gas occupies all of the larger pores. Throughout the entire range of depths, water occupies the smallest pores.

For a three-phase system, the capillary pressure of each phase is a function of the specific distribution of pore sizes that the hydrate and gas phases actually occupy. The figure above shows how each phase will occupy different pore sizes given a lognormal distribution. Since the gas fills the largest pore sizes first, any given S_g will occupy all pore sizes greater than some pore radius r_g. Therefore, the gas capillary pressure is only a function of S_g. Hydrate fills the next largest pore sizes, so we must take into account that the largest pore sizes have already been occupied with gas. A given S_h will occupy pore sizes that are greater than r_h and less than r_g; this is identical to the two-phase situation where all of the pore sizes that are filled with gas are instead filled with hydrate. Thus, when calculating the hydrate capillary pressure, we see both S_g and S_h as the combined non-wetting saturation and sum the two together (Leverett, 1941):

$$P_{c,gw}^{3P} = P_{c,gw}^{2P}(S_g) \tag{3.7}$$

$$P_{c,hw}^{3P} = P_{c,hw}^{2P}(S_g + S_h) \tag{3.8}$$

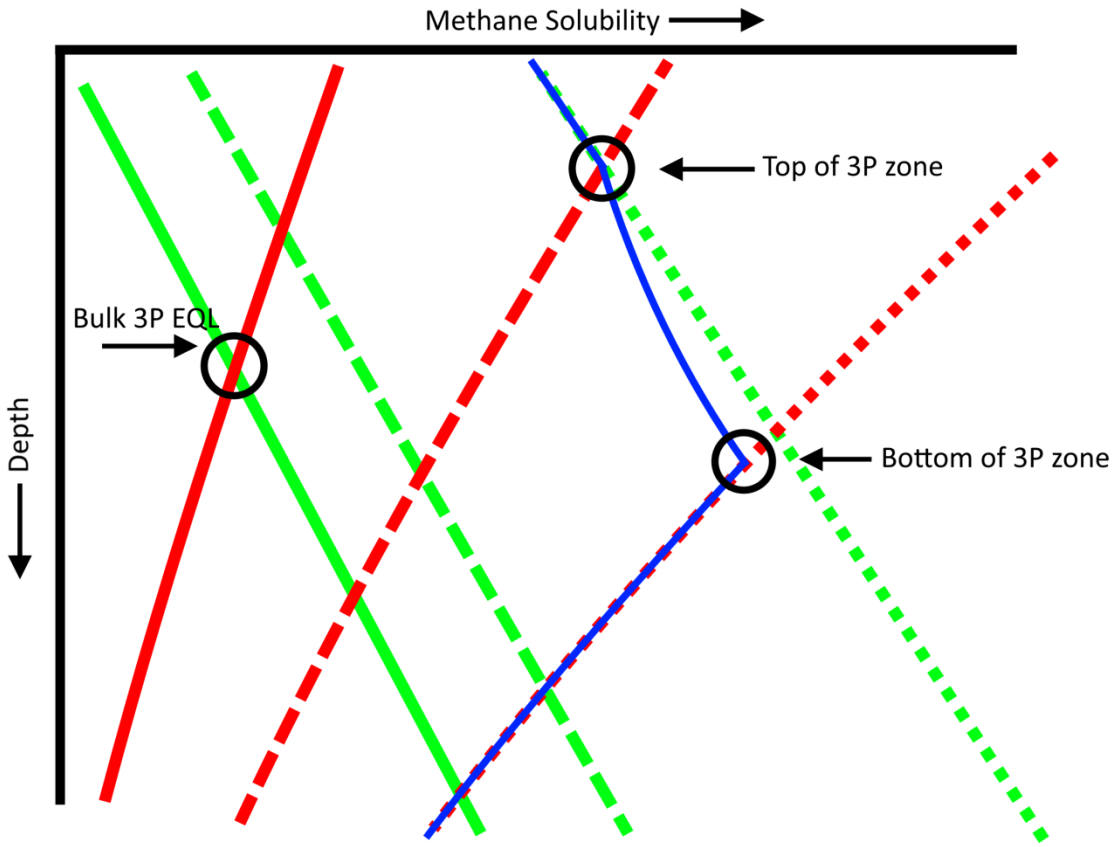

Figure 3.2 Example schematic of methane solubility curves for a given constant methane quantity. The hydrate-water solubilities are shown in green, and the gas-water solubilities are shown in red. Red and green solid lines represent bulk solubility. Dashed lines represent the minimum solubility, which are elevated from bulk solubility because of the capillary entry pressure of the non-wetting phase. Dotted lines represent the maximum solubility for a two-phase system at some non-wetting saturation, which is also a function of the methane quantity. The blue solid line is an example of the system's actual methane concentration in the two-phase and three-phase zones. Within the three-phase zone, the calculated blue line represents the solubility due to the smallest non-wetting phase-filled pore. Note that this schematic's minimum solubility curves are shown as relatively larger than the bulk solubility curves. This is for graphical purposes only; usually, the capillary entry pressures are not large enough to cause a substantial solubility elevation from bulk solubility.

We now cover the calculation of saturations for three-phase stability. The following algorithm can be conceptualized as flash calculation to solve for the hydrate and gas saturation. We use the mass balance equation for methane again, and this time methane can be a component of all three phases:

$$S_w \rho_w C_{CH_4} + S_h \rho_h f_{CH_4} + S_g \rho_g = M_{CH_4} \tag{3.9}$$

$$S_w + S_h + S_g = 1 \tag{3.10}$$

$$C_{CH_4} = C_{G-W} = C_{G-H} \tag{3.11}$$

The condition for three-phase stability is that the gas-water solubility must equal the hydrate-water solubility. This is possible because capillary effects can elevate the solubility of each system by different magnitudes to meet equality.

First, we locate the top of the three-phase transition zone. Above this, methane is either contained in hydrate or dissolved in water. Basically, the layer above the three-phase zone is treated like a two-phase system with added capillary effects.

We iteratively calculate the equilibrium methane solubility of a hydrate-water system, which is elevated from bulk solubility due to the smallest pore size that the hydrate phase occupies. This methane solubility represents the maximum solubility (C_{H-W}^{Max}) that can be reached in a hydrate-water system for a given methane quantity. Through this iteration, we also find the hydrate saturation, which is less than what we would calculate if bulk solubility was assumed; this is due to the elevated C_{H-W}^{Max} allowing the water phase to dissolve more methane from the hydrate.

We also calculate the minimum methane solubility (C_{G-W}^{Min}) of a gas-water system. This is the solubility, elevated from bulk solubility, when we assume that the pore space

is fully saturated with water ($S_w = 1$), and the gas phase is on the verge of forming. Here, the capillary entry pressure of gas plays a role. Since the capillary entry pressure increases the first bubble of gas's pressure above hydrostatic, methane solubility is elevated above bulk solubility to some degree, even though there is no substantial gas phase present yet. We conceptualize this as the following. If the water phase (at $S_w = 1$) is supersaturated at bulk solubility, adding an infinitesimally small amount of methane will form the gas phase. The gas fills the largest pore, and which induces capillary pressure and elevates the solubility of the system. This causes that first gas bubble to dissolve back into water at equilibrium.

The top of the three-phase zone is where $C_{G-W}^{Min} = C_{H-W}^{Max}$. At this condition, the gas-water system is supersaturated and is on the brink of forming the first gas bubble. At the same time, the hydrate-water system is also supersaturated and all the excess methane forms hydrate, which fills large pores down to some discrete pore size. Above this depth, no gas is present, and the hydrate saturation is as previously calculated when iterating for C_{H-W}^{Max}. Below this depth, the change in pressure and temperature will cause some of the methane to change phases and form gas in the largest possible pore.

For the depths within three-phase stability, we also iteratively calculate the three-phase saturations. Throughout the three-phase zone, gas-water solubility must be equal to hydrate-water solubility. This condition allows us to perform a flash-style calculation. We first guess S_g and use mass balance to find S_h. We also need to guess the methane solubility of the three-phase system. From S_g and S_h, we calculate the elevated solubility of both systems by using the three-phase capillary pressures. Using Newton-Raphson iteration, we solve for the set of saturations that conserve mass and fulfill the equal solubility condition. As we move deeper into the three-phase stability zone, more methane partitions into the gas phase, and less of the methane partitions into the hydrate

phase. Because of our interfacial energy minimization assumption, gas occupies the largest pore sizes while hydrate occupies the smaller pore sizes. The water phase stays supersaturated with methane throughout the entire three-phase zone.

The bottom of the three-phase zone is found by comparing the solved system methane solubility with the max solubility (C_{G-W}^{Max}) of a gas-water system. We calculate C_{G-W}^{Max} in the same manner as we do for C_{H-W}^{Max}; assuming no hydrate forms, we iteratively calculate the methane solubility while adjusting for capillary effects. The gas capillary pressure increases the solubility of the water phase, decreasing the gas saturation relatively to bulk conditions. As before, we also simultaneously calculate the associated gas saturation of the gas-water system.

The bottom of the three-phase zone, the calculated system methane solubility equals C_{G-W}^{Max}, and the hydrate saturation naturally approaches zero. At this depth, the solubility elevation caused by the near-zero hydrate saturation in the smaller pore size is the same as the solubility elevation due to gas occupying all the larger pores down to that same smaller pore size. Thus, when that hydrate saturation actually becomes zero, there is no discontinuity in the calculated capillary pressures, solubilities, and saturations. We model the layer below the three-phase zone as a two-phase gas-water system, because the gas phase is more stable than hydrate at these depths. The lower gas layer is characterized with C_{G-W}^{Max} and the corresponding gas saturation.

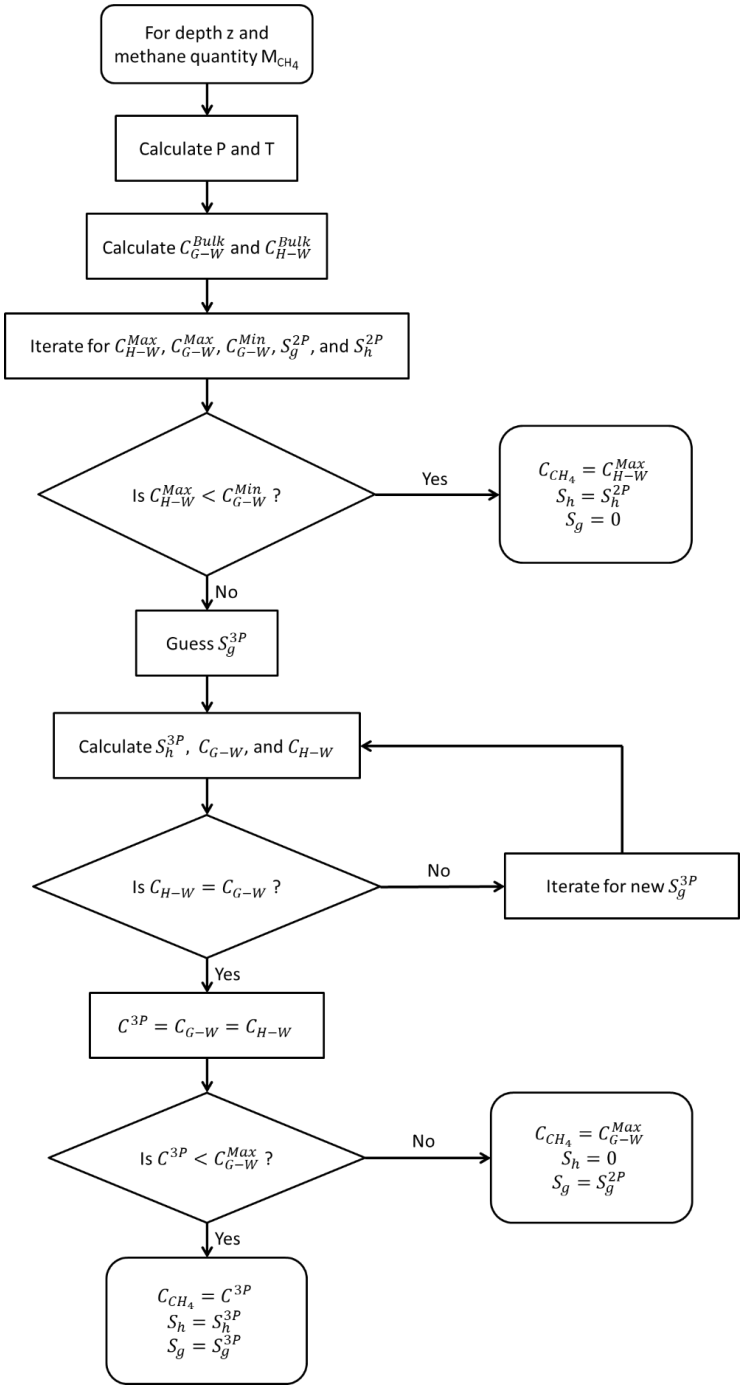

Figure 3.3 Algorithm flowchart for the phase saturation calculation for the three-phase stability model.

3.2 ROCK PHYSICS MODEL

To generate synthetic seismograms, we create a 1-D rock physics model from existing well log data that allows us to calculate rock and fluid properties from the seafloor to below the BGHS. We build this rock physics model using a one meter depth increment. The following analysis is done for Ocean Drilling Program Site 995 at Blake Ridge, so portions of our model include empirical formulas because the well log data is site-specific. Our rock physics model is constructed using Gassmann fluid substitution (Gassmann, 1951).

3.2.1 Fluid Substitution

For our fluid substitution algorithm, we need saturation-depth profiles for the hydrate, gas, and water phases. We obtain these saturation profiles by using our three-phase stability model previously described in section 3.1.2. For the rest of the fluid substitution workflow, we follow the workflow described in Guerin et al., (1999), which used fluid substitution to investigate seismic and fluid properties at Blake Ridge. The objective of our rock physics model is to calculate fluid substituted bulk densities and compressional wave velocities. To achieve this, we use the following input data to set the required rock properties needed for fluid substitution: the bulk density log, velocity logs, gamma ray log, and deep resistivity log from Site 995.

Normally, porosity is can be estimated using the density porosity and neutron porosity logs. However, the specific well logs that we use (see section 5.1.2) show that much of the logged interval had poor contact between the logging tool's caliper arms and the borehole (Guerin et al., 1999). This was likely caused by poor wellbore quality, which is common in shallow, unlithified sediments near the seafloor. Poor wellbore quality is

often detrimental to density porosity and especially neutron porosity data quality. Thus, we calculated the porosity using Archie's law:

$$\phi = \left[a\left(\frac{R_w}{R_t}\right)\left(\frac{1}{{S_w}^n}\right)\right]^{m^{-1}} \tag{3.12}$$

where R_w is the brine resistivity, R_t is the formation resistivity, and S_w is the water saturation. Shipboard Scientific Party (1996) determined Archie parameters $a = 0.9$ and $m = 2.7$ from log data, and Pearson et al. (1983) determined $n = 1.94$ from multiple laboratory resistivity experiments of partially-frozen sediments. We use the deep resistivity from the resistivity log as R_t. Guerin et al. (1999) used the following empirical formula to calculate R_w:

$$R_w = R_{wo}\left(\frac{T_o + 21.5}{T + 21.5}\right) \tag{3.13}$$

where R_{wo} is the resistivity of seawater of salinity, which is similar to the formation brine salinity, measured at a reference temperature of T_o. The variation with depth of the in situ sediment temperature T was determined from a temperature gradient of 38.5°C/km and a seafloor temperature of 3°C (Shipboard Scientific Party, 1996). We take R_{wo} to be 0.24 ohm-m for a reference temperature of 18°C (Schlumberger Limited, 2000). To estimate S_w, we use an empirical relationship between R_o, the resistivity of water-saturated sediment, and R_t. For our specific set of well logs, a linear fit for R_o was previously developed by matching the salinity variation with depth z (in meters below seafloor) with the measured resistivities (Paull et al., 1996; Collett and Ladd, 2000). After substituting the linear trend for R_o, we have:

$$S_w = \left(\frac{2.986 \times 10^{-4}(z) + 0.8496}{R_t}\right)^{n^{-1}} \tag{3.14}$$

Since porosities at Site 995 are generally greater than 0.50 (Guerin et al., 1999), we do not expect that reduced resistivity, commonly contributed by clay mineral surfaces, to affect the porosity calculation; this effect only tends to be significant for marine sediments with porosity less than 0.30 (Erickson and Jarrard, 1998).

The bulk modulus of the formation is calculated with compressional and shear velocity and bulk density from the velocity and density logs (Mavko et al., 2009):

$$K_{bulk} = \rho_{bulk}\left(V_p^2 - \frac{4}{3}V_s^2\right) \tag{3.15}$$

We obtain the bulk density from the density porosity log. While we avoided using the density porosity log with the neutron porosity log to calculate the actual porosity because of rugose hole conditions, we still use the raw bulk density data from the density porosity log because the bulk density data was uniformly 0.1 g/cm^3 less than the shipboard-measured bulk density (Guerin et al., 1999). This difference is only 6% of the total bulk density and does not significantly affect later calculations.

We use the gamma ray log to estimate sediment clay abundance to account for the effect of clays on the elastic moduli. We normalize the spectral gamma ray values to estimate the clay content fraction of the sediment by mapping the clay fraction γ from 0 (clay-free) to 1 (pure clay) to gamma ray values between 12 API and 110 API. This aligns the normalized gamma ray values with the clay content fraction seen in smear slide tests (Paull et al., 1996). We use the normalized gamma ray values to calculate the apparent grain bulk modulus using the Voigt-Reuss-Hill averaging method (Hamilton, 1971):

$$K_{grain} = \frac{1}{2}\left[\gamma K_c + (1-\gamma)K_s + \frac{K_s K_c}{\gamma Ks\ +\ (1-\gamma)K_c}\right] \tag{3.16}$$

where K_s is the sand grain modulus, taken as 38.4 GPa which is the value for quartz (Pabst and Gregorová, 2013). The clay grain modulus K_c is 21.2 GPa (Guerin et al., 1999; Lee et al., 1996; Mavko et al., 2009).

Our rock physics model establishes the frame modulus of the sediment from the existing well log data, and our model requires an assumption of the hydrate phase's pore habit. The pore habit is how the hydrate phase naturally forms or resides in the pore space spatially; this has implications on how the hydrate phase affects the elastic properties of the porous sediment. For instance, hydrate that directly cements rock grains together can greatly increase the sediment shear and dry frame stiffness (Dvorkin et al, 1999). From our previously established three-phase stability pore model, we assume that the hydrate is pore-filling, following how Clennell et al. (1999) characterized gas hydrates as small crystals dispersed within the pore space of the sediment. Previous amplitude versus offset (AVO) analysis at Blake Ridge concluded that the hydrate phase resides only in the pore bodies, instead of cementing rock grains and providing structural support (Ecker et al., 1998). On the other hand, Waite et al. (2009) and Dai et al. (2012) characterized the Blake Ridge hydrate phase pore habit as nodules, where hydrate completely fills regions of the pore space and becomes part of the load-bearing framework. In general, the hydrate phase pore habit is predicted to be pore-filling when the hydrate saturations are less than 25% - 40% and load-bearing when the hydrate saturations are greater than the given range (Waite et al., 2009; Dai et al. 2012). For the range of methane quantities that we investigate with our rock physics model, the calculated hydrate saturations do not exceed 40%. Thus, we model all methane quantity cases as pore-filling. We use this assumption in our rock physics model by making the frame modulus independent of the hydrate saturation.

Hamilton (1971) developed experimental correlations between porosity and the frame modulus of silty clays and fine sands. Guerin et al. (1999) expanded these correlations by including the effect of the grain modulus for the sediments at Site 995:

$$K_{frame} = K_{grain} \times 10^{(3.02-7.372\phi)} \tag{3.17}$$

The fluid modulus is approximated by the isostress average, which is the volume-weighted harmonic mean:

$$K_{fluid} = \frac{1}{\frac{S_w}{K_w} + \frac{S_g}{K_g} + \frac{S_h}{K_h}} \tag{3.18}$$

where K_w is the bulk modulus of water, and K_h is the bulk modulus of gas hydrate, with values of 2.688 GPa (Guerin et al., 1999) and 8.4 GPa (Helgerud et al., 2009), respectively. To calculate the bulk modulus of gas K_g, we use the equation of state from Batzle and Wang (1992), which accounts for both changing pressure and temperature. The bulk modulus of gas is approximated by the hydrostatic pressure P and temperature T of the formation at depth:

$$K_g = \frac{c'P}{\left(1 - \frac{P}{Z}\frac{\partial Z}{\partial P}\right)_T} \tag{3.19}$$

where c' is the ratio of the heat capacity at constant pressure to the heat capacity at constant volume, and Z is the compressibility factor. This formulation predicts a gas bulk modulus approximately 2 to 4 times higher than what we expect for an ideal gas; this is likely because of Blake Ridge's relatively deep seafloor and higher hydrostatic pressures for a hydrate-bearing formation.

Guerin et al. (1999) calls the combination of rock models from Gassmann (1951) and Hamilton (1971) the Gassmann/Hamilton model, which relates the rock's grain modulus, frame modulus, fluid modulus, and porosity to the rock's bulk modulus. We use

the Gassmann/Hamilton model to obtain the bulk modulus $K_{bulk,fs}$ of our fluid substituted rock physics model:

$$Q = \frac{K_{fluid}\left(K_{grain} - K_{frame}\right)}{\phi\left(K_{grain} - K_{fluid}\right)} \tag{3.20}$$

$$K_{bulk,fs} = K_{grain}\frac{K_{frame} + Q}{K_{grain} + Q} \tag{3.21}$$

Lastly, the shear modulus G is determined from the shear velocity log and bulk density log measurements (Mavko et al., 2009):

$$G = \rho_{bulk}V_s^2 \tag{3.22}$$

3.2.2 Synthetic Seismogram Generation

The following procedure calculates the fluid substituted seismic velocity and bulk density. These values are subsequently averaged over some depths of interest, namely the layer above and below the three-phase stability zone.

The fluid substituted bulk density is calculated from weighted averages of data using the gamma ray log, phase saturation profile, and estimated porosity:

$$\rho_{fluid,fs} = S_w\rho_w + S_g\rho_g + S_h\rho_h \tag{3.23}$$

$$\rho_{matrix} = \gamma\rho_{clay} + (1 - \gamma)\rho_{sand} \tag{3.24}$$

$$\rho_{bulk,fs} = \phi\rho_{fluid,fs} + (1 - \phi)\rho_{matrix} \tag{3.25}$$

For quartz and clay endpoint grain density, we use 2.65 g/cm^3 and 2.7 g/cm^3, respectively. Using the fluid substituted bulk density, we calculate the fluid substituted shear wave velocity by holding the shear modulus constant:

$$V_{s,fs} = \sqrt{\frac{G}{\rho_{bulk,fs}}} \tag{3.26}$$

Likewise, we obtain the fluid substituted compressional wave velocity from the fluid substituted bulk modulus and fluid substituted bulk density (Mavko et al., 2009):

$$V_{p,fs} = \sqrt{\frac{K_{bulk,fs}}{\rho_{bulk,fs}} + \frac{4}{3}V_{s,fs}^2} \tag{3.27}$$

We calculate the impedance I for each depth using the average fluid substituted bulk densities and compressional wave velocities:

$$I = \rho_{bulk,fs}V_{p,fs} \tag{3.28}$$

The reflection coefficient R is calculated from the change in impedance from one layer to the next:

$$R_{i,i+1} = \frac{I_{i+1} - I_i}{I_{i+1} + I_i} \tag{3.29}$$

The reflectance of each layer transition constitute a reflectivity versus depth series. We convert the each depth to two way travel time (TWTT) by dividing the depth increment by the fluid substituted compressional wave velocities. We finally convolve the reflectivity series in TWTT with a 30 Hz, zero-phase Ricker wavelet to generate the synthetic seismogram. By varying the methane quantity, we can create a range of three-phase saturation profiles and generate a synthetic seismogram for each methane quantity with this workflow.

For this work, we make two rock physics models for analysis. The first is the parameter sensitivity model, where we initially average the background rock properties from the well log data across the three-phase stability zone. These parameters are held constant around the three-phase zone before doing fluid substitution. The second model is

the original-resolution rock physics model, where we use the background rock properties as is for the fluid substitution. For both rock physics models, we want to highlight the effect of the three-phase zone. To do this, we upscale all the depths outside of the three-phase zone into two layers over which the fluid substituted bulk densities and sonic velocities are averaged. The upper hydrate layer extends upward from the BSR, and the lower gas layer extends downward from the BGHS. We set the thicknesses of the upper hydrate layer and lower gas layer to one seismic wavelength of the seismic wave traveling through each layer. These thicknesses change slightly with saturation profiles due to the corresponding changes in seismic velocities.

Chapter 4: Gas Overpressure Initiating Fractures

In this chapter, we compare the gas overpressure that arises from the three-phase bulk equilibrium model and the three-phase stability model. Since these two models solve for phase saturations differently, there should be relevant effects from capillary pressure in pores that alter how one might model gas overpressure on basin scales.

We apply our models in conjunction with MICP data from three different hydrate-bearing basins. We calculate three-phase saturations and methane solubilities in and around three-phase stability. We use this to model the gas overpressure due to gas capillary pressure, and we compare the gas overpressure against the minimum horizontal effective stress to determine if hydraulic fractures are initiated. We also investigate how differing seafloor depths affect the gas overpressure behavior.

4.1 DATA

For this study, we focus on three hydrate-bearing locations: Ocean Drilling Program (ODP) Site 995 at Blake Ridge, ODP Site 1250 at Hydrate Ridge, and Integrated Ocean Drilling Program (IODP) Site C0002 at Kumano Basin. Various types of data were gathered from these three wells, and we summarize the data necessary for our model calculations.

4.1.1 Model Parameters

In order to calculate hydrate, gas, and water saturations, we require the pressures and temperatures to be known at every depth. To accomplish this, we estimate pressures and temperatures from available gradient data in the literature. Salinity is assumed to be seawater salinity. The reservoir properties for Blake Ridge, Hydrate Ridge, and Kumano Basin are compiled in the table below.

	Blake Ridge, ODP Site 995	Hydrate Ridge, ODP Site 1250	Kumano Basin, IODP Site C0002
Seafloor depth (m)	2780	790	1936
Seafloor temperature (°C)	3.3	4	2.2
Temperature Gradient (°C/km)	36.9	59	40
Salinity (weight percent)	3.5	3.5	3.5
References	Ruppel (1997), Henry et al. (1999)	Tréhu (2006)	Expedition 314 Scientists (2009), Expedition 315 Scientists (2009)

Table 4.1 Reported reservoir properties used for modeling three-phase saturations. Adapted from Liu and Flemings (2011).

4.1.2 Mercury Intrusion Capillary Pressure

We use available MICP data from Blake Ridge (Henry et al., 1999), Hydrate Ridge (Liu and Flemings, 2011), and Kumano Basin (Dugan, 2015). The MICP data is shown in the figure below. The samples from Hydrate Ridge and Kumano Basin show relatively similar inferred pore size distributions. There are two samples from Blake Ridge, and both MICP curves reveal a great volume of large pore sizes and low capillary entry pressures. This is likely due to the significant presence of diatoms within the sediment (Kraemer et al., 2000). Because the samples from Blake Ridge are quite abnormal, we do not fit previously discussed capillary pressure models to the MICP. Instead, we choose to interpolate directly from the MICP data the capillary pressure for any non-wetting saturation.

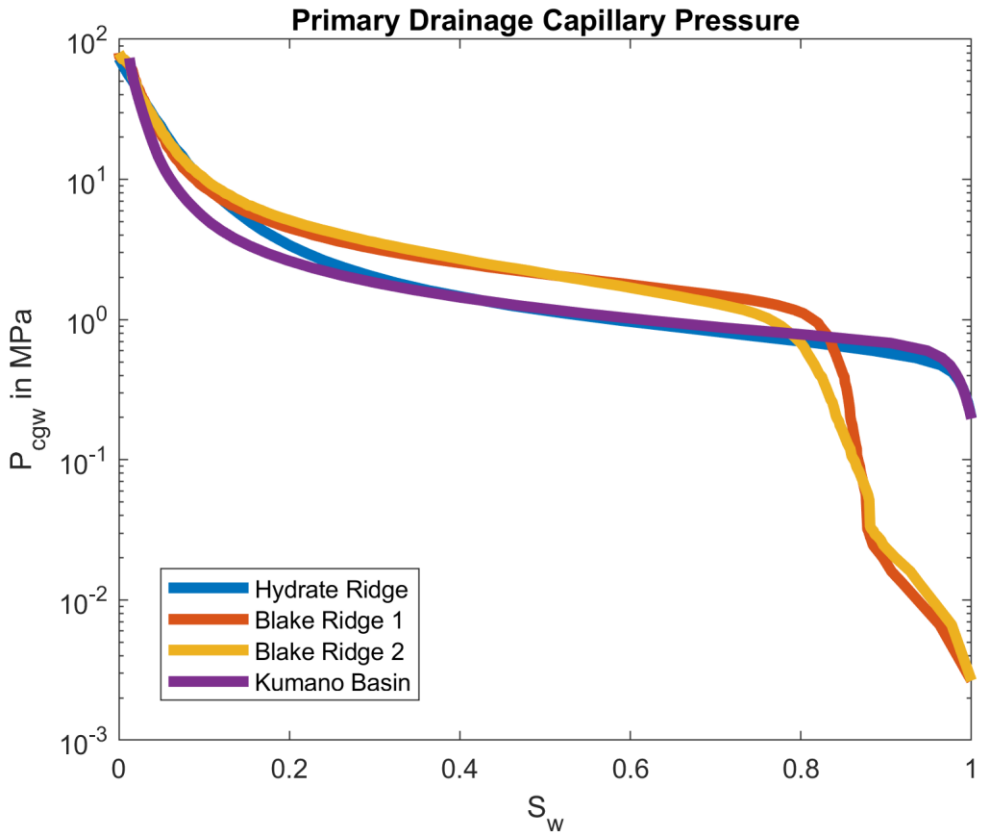

Figure 4.1 Mercury intrusion capillary pressure (MICP) data, converted into gas-water capillary pressure.

4.1.3 In-Situ Methane Quantity

The Pressure Core Sampler (PCS) system was used to measure in situ methane quantities at Blake Ridge ODP Site 995 and 997, and results indicated a maximum methane quantity near 40 kg/m^3 of pore volume (Dickens et al., 1997b). For our modeling purposes, we choose methane quantity to be a constant 40 kg/m^3 for all depths; this makes for smooth solubility and saturation curves and provides enough methane to supersaturate the water phase. This assumption is also taken in Liu and Flemings (2011), and we also bring the constant 40 kg/m^3 methane quantity to Hydrate Ridge and Kumano Basin.

For Hydrate Ridge ODP Site 1250, resistivity-at-bit (RAB) measurements estimate a maximum hydrate saturation of 26% (Tréhu et al., 2004). Modeling hydrate saturations from the combination of logging-while-drilling (LWD) deep resistivity and chloride concentration data estimates hydrate saturations from 20% to 40% (Liu and Flemings, 2006). Our model produces hydrate saturations around 30% in the hydrate-bearing layer when we use 40 kg/m^3 as the methane quantity.

For Kumano Basin IODP Site C0002, hydrate saturation estimates using P-wave velocity logs and LWD resistivity derive hydrate saturations of approximately 30% (Miyakawa et al., 2014). Our model produces hydrate saturations of 30% when using 40 kg/m^3 as the methane quantity, so we find our usage of constant 40 kg/m^3 to be reasonable.

4.2 RESULTS

After combining all the required data, we calculate phase saturations and methane solubilities for the three locations using the model algorithm previously described. The hydrate and gas saturation for both the three-phase bulk equilibrium model and the three-phase stability model are shown in the following sections, along with the methane system solubilities.

4.2.1 Blake Ridge

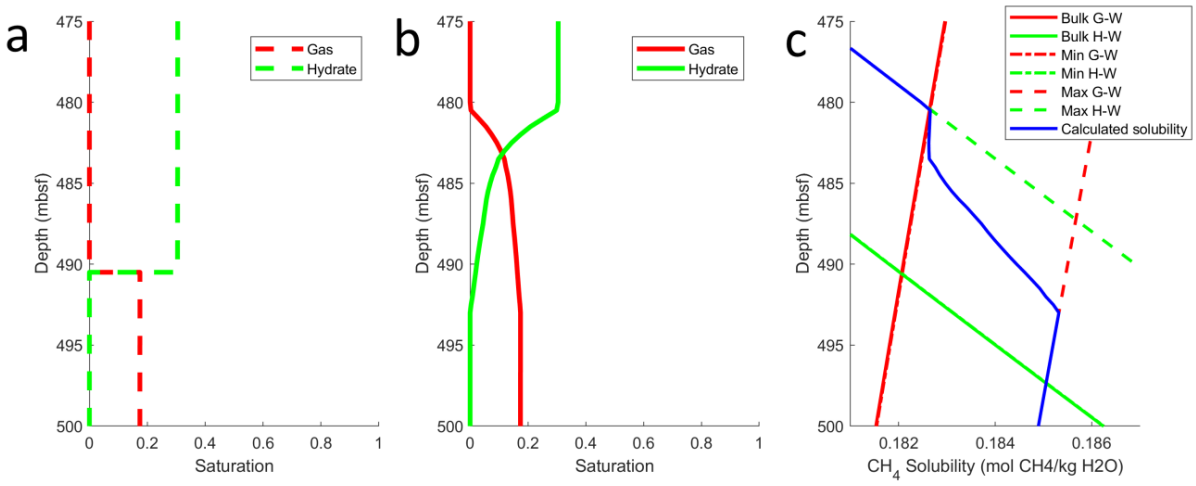

Figure 4.2. Results for ODP Site 995, showing a) three-phase bulk equilibrium model phase saturations, b) three-phase stability model phase saturations, and c) calculated methane solubility curves.

The three-phase bulk equilibrium model calculates hydrate saturations above z_{3P}^{Bulk} and gas saturations below z_{3P}^{Bulk}. The saturations may seem constant in depth, but both phase saturations decrease as depth increases. The hydrate saturation decreases with depth because the hydrate-water methane solubility increases with depth; this allows more methane to dissolve into water to maintain supersaturation. The gas saturation decreases with depth because gas density increases with depth.

The three-phase stability model shows the hydrate saturation smoothly declining while the gas saturation builds up, as we move from top to bottom of the three-phase zone. The three-phase stability model predicts a significant amount of gas saturation above z_{3P}^{Bulk}, due to the significant amount of large pores in the pore size distribution. The gas density is relatively high because of Blake Ridge's deep seafloor depth, so the methane quantity in the gas phase takes up less space than the same methane quantity in the hydrate phase.

The bulk solubility curves, used for the bulk equilibrium model, intersect around 490.5 meters below seafloor (mbsf). The capillary entry pressure of the Blake Ridge samples are magnitudes lower than the capillary entry pressures seen at Hydrate Ridge and Kumano Basin, so the minimum solubility curves are barely elevated above bulk solubility. Because of this, C_{G-W}^{Min} and C_{H-W}^{Max} intersect at approximately 10 meters above z_{3P}^{Bulk}. The thickness of the three-phase zone is approximately 13 meters. Due to the large amount of larger pores in Blake Ridge's pore size distribution, significant gas saturation can form in the larger pore sizes near the top of the three-phase zone. Since these larger pores constitute a significant fraction of the total pore volume, the calculated methane solubility in the three-phase zone pulls away from C_{H-W}^{Max}. As we move deeper into the three-phase zone, the gas phase begins to invade smaller pores, so we see the shift in the calculated methane solubility from hugging the C_{G-W}^{Min} curve to moving towards the C_{G-W}^{Max} curve.

4.2.2 Hydrate Ridge

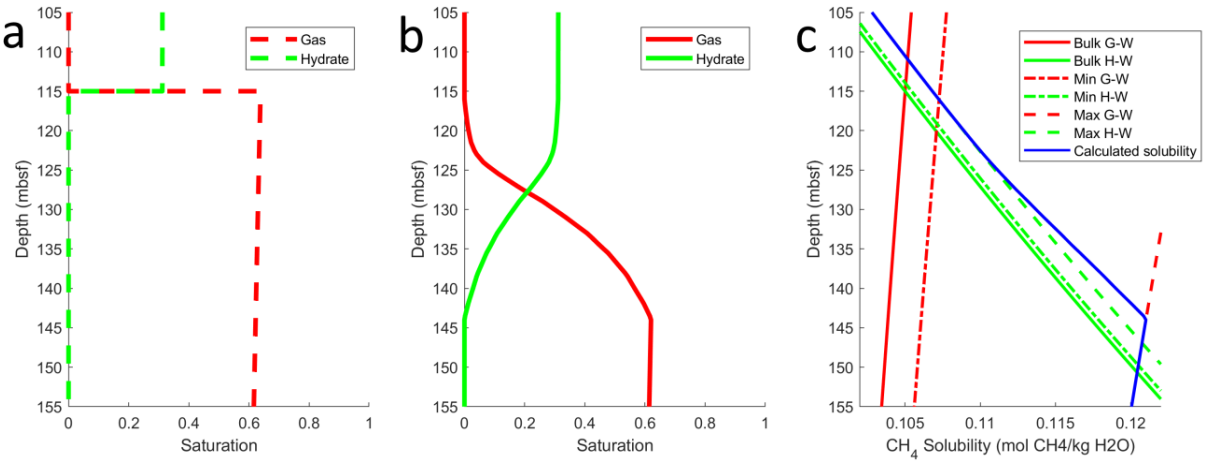

Figure 4.3 Results for ODP Site 1250, showing a) three-phase bulk equilibrium model phase saturations, b) three-phase stability model phase saturations, and c) calculated methane solubility curves.

The gas saturations at Hydrate Ridge are much higher than at Blake Ridge, even though we use the same methane quantity for all locations. Hydrate Ridge's shallower seafloor depth causes the pore pressures to be much smaller in magnitude than the pore pressures at Blake Ridge. Thus, the gas density at Hydrate Ridge is much less than the gas density at Blake Ridge, so the same amount of methane will occupy much of the more pore volume at Hydrate Ridge. For the three-phase stability model, the behavior of Hydrate Ridge's saturation curvature is representative of a more natural saturation transition zone, compared to Blake Ridge. The saturations show a steady change from top to bottom, and both the hydrate and gas saturation curves have inflection points; this is not the case at Blake Ridge, where the saturation curves are only concave down.

The methane solubility curves for Hydrate Ridge show much different behavior compared to Blake Ridge. The C_{G-W}^{Min} curve is much more elevated above bulk solubility, which causes the top of the three-phase zone to occur at a deeper depth. This brings the

top of the three-phase zone close to z_{3P}^{Bulk} at 115 mbsf. Additionally, there is greater separation between C_{G-W}^{Min} and C_{G-W}^{Max}. This happens because the gas density at Hydrate Ridge is relatively low; larger gas saturations allow the gas phase to invade more of the smaller pores, increasing the gas capillary pressure and thus increasing the maximum gas-water solubility. Because of this, the three-phase stability zone spans almost 28 meters for a constant methane quantity of 40 kg/m^3. The separation between C_{H-W}^{Min} and C_{H-W}^{Max} is much smaller in comparison to the gas-water solubilities, whereas at Blake Ridge, the separation between minimum and maximum solubilities are closer in magnitude.

4.2.3 Kumano Basin

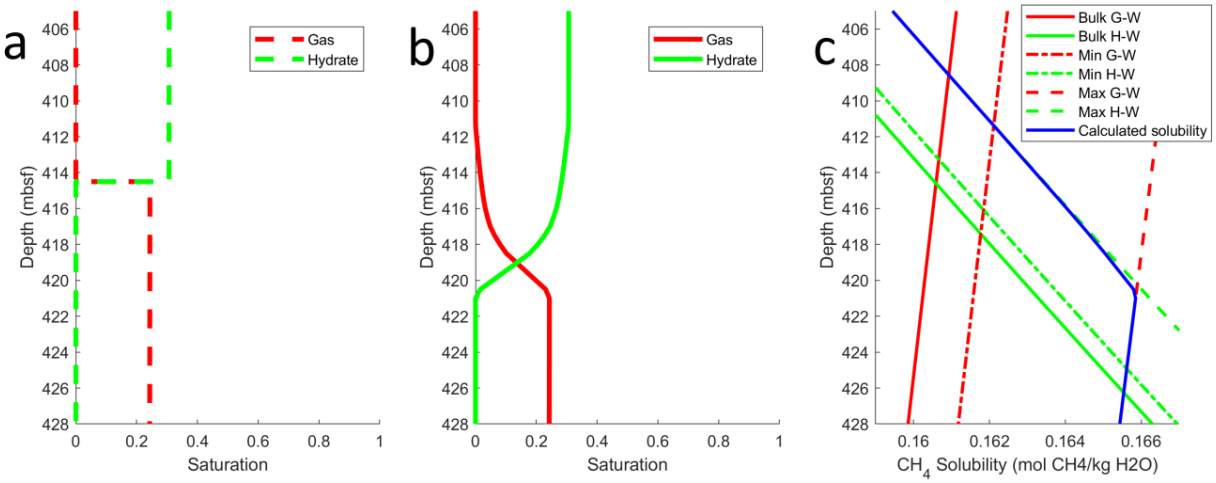

Figure 4.4 Results for IODP Site C0002, showing a) three-phase bulk equilibrium model phase saturations, b) three-phase stability model phase saturations, and c) calculated methane solubility curves.

Kumano Basin is unique because it has a pore size distribution similar to Hydrate Ridge's, while having a deep seafloor depth like Blake Ridge. The three-phase bulk equilibrium model's phase saturations at Kumano Basin show similar trends to that at

Blake Ridge. While the seafloor depth of Kumano Basin is not as deep as Blake Ridge's seafloor depth, the higher gas density results in similar gas saturations.

The three-phase stability saturations at Kumano Basin are similar in curvature to Hydrate Ridge because of the similar pore size distributions. However, the gas saturations are much lower in magnitude than Hydrate Ridge's gas saturation. Interestingly, the total non-wetting saturation ($S_g + S_h$) stays relatively constant throughout the three-phase zone.

For Kumano Basin, we see smaller separations between bulk, minimum, and maximum solubilities. The separation between hydrate-water solubility curves is less in magnitude than the separation between gas-water solubility curves. The top of the three-phase zone is around 3 meters above the z_{3P}^{Bulk}. The three-phase zone's thickness is approximately 9 meters. Throughout the three-phase zone, the calculated methane solubility closely follows the C_{H-W}^{Max} curve; this happens because the total non-wetting saturation stays nearly constant within three-phase zone. As long as the total non-wetting saturation stays constant, the smallest pore size that the hydrate phase invades will also stay constant ($S_h + S_g = 1 - S_w$).

4.3 DISCUSSION

4.3.1 Gas Overpressure

We investigate the gas overpressure for both phase saturation models for Blake Ridge, Hydrate Ridge, and Kumano Basin. Using the previously described fracture criterion, we directly compare the gas capillary pressure against the minimum horizontal effective stress. If the gas capillary pressure exceeds the minimum horizontal effective stress, then the gas can theoretically initiate a fracture. Gas overpressure increases as gas saturation increases, and the minimum horizontal effective stress increases as depth

increases since the overburden grows with depth. We show a simplified form of the overpressure ratio, which we define as the gas overpressure divided by the minimum horizontal effective stress. By doing this, we can make a depth-by-depth comparison of the overpressure of both saturation models; if the ratio exceeds unity, then a fracture can be initiated.

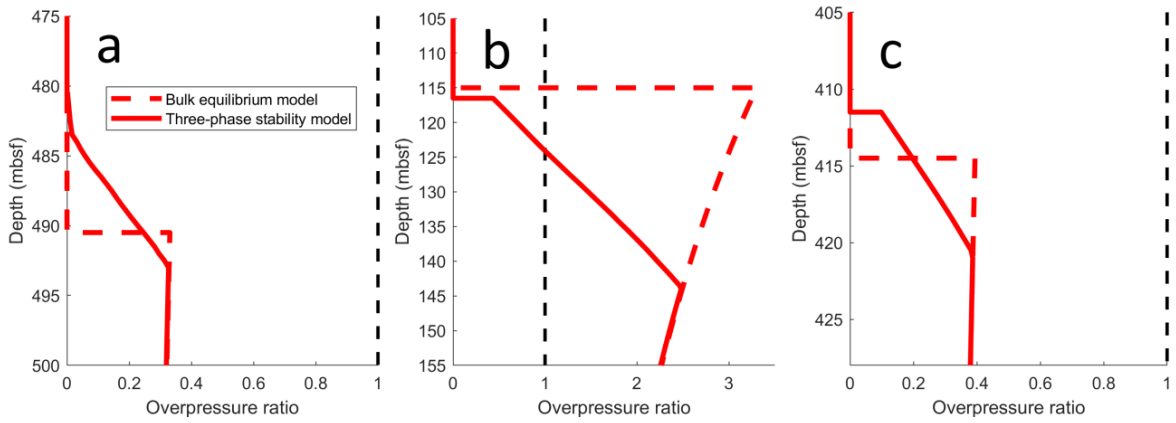

Figure 4.5 Gas overpressure ratio for a) ODP Site 995, b) ODP Site 1250, and c) IODP Site C0002. The overpressure ratio is the gas overpressure divided by the minimum horizontal effective stress. If the overpressure ratio exceeds unity, then a fracture can initiate. Note that, below the bottom of the three-phase stability zone, the overpressure ratios of the two models are not overlapping; the three-phase stability model has slightly smaller gas saturations in the two-phase gas-water layer because of the higher solubility due to capillary effects. Thus, the smaller gas saturation generates less overpressure compared to the three-phase bulk equilibrium model.

For Blake Ridge, we see that the deep seafloor depth and high gas density greatly lower the gas overpressure by reducing the gas saturation that a given methane quantity can achieve. Below the bottom of the three-phase stability zone, we note that the bulk equilibrium model predicts slightly higher gas saturations than the three-phase stability model. Additionally, the deep formation depth equates to larger minimum horizontal effective stresses, which further reduces the overpressure ratio.

At Hydrate Ridge, the seafloor and formation depths are much shallower than at Blake Ridge and Kumano Basin, so the overpressure required to exceed the minimum horizontal effective stress is much less. When we model with a methane quantity of 40 kg/m^3, the minimum horizontal effective stress is easily exceeded. It is important to note that our overpressure models only predict the initiation of a hydraulic fracture, not the propagation of a fracture. As in the case of Hydrate Ridge, once enough methane quantity accumulates over time to initiate a fracture, the gas phase would naturally migrate up the fracture. Our modeling does not account for this because the system would no longer be in at equilibrium.

The overpressure at Kumano Basin follows similar trends to that seen at Blake Ridge. Like Blake Ridge, Kumano Basin shows that the three-phase stability model can predict overpressures above z_{3P}^{Bulk}. For Kumano Basin, this overpressure occurs from about 411.5 mbsf to 414.5 mbsf. This happens because the gas saturation within the three-phase zone transitions to zero at the top due to capillary effects. Since the gas saturation decreases as we move shallower towards the top of the three-phase zone, it is unlikely that this gas overpressure will initiate a fracture if the gas overpressure at the bottom of the three-phase zone did not already do so. For this to happen in our model, the lithology would have to change over depth in order to have large changes in minimum horizontal effective stresses. Another way our model can investigate the significance of the overpressures above z_{3P}^{Bulk}would be to have methane quantities that vary with depth. For this portion of the work, we assume that the methane quantity is given and is constant over all depths; in application, the methane quantities can vary significantly, especially at depths close to z_{3P}^{Bulk} (Dickens et al., 1997b). While our algorithm can calculate phase saturations for both the three-phase bulk equilibrium model and the three-phase stability model on a depth-by-depth basis, we did not include that in this section due to the relative

scarcity of PCS methane quantity measurements over a large range of depths at Hydrate Ridge and Kumano Basin to make this analysis appropriate.

For all three locations, the three-phase bulk equilibrium model predicts higher gas overpressures because of two reasons: 1) the bulk solubility is always less than the solubility when accounting for capillary effects, and 2) the depth of three-phase bulk equilibrium lies above the bottom of the three-phase zone. Since capillary effects always elevate the system's methane solubility, the three-phase stability model's gas saturations are always slightly less than the three-phase bulk equilibrium model's gas saturations, for an equal amount of methane quantity. Additionally, the bottom of the three-phase zone is deeper than z_{3P}^{Bulk}. The maximum gas saturation for the bulk equilibrium model occurs at z_{3P}^{Bulk}, and the maximum gas saturation for the three-phase stability model is at the bottom of the three-phase zone. This means that the three-phase stability model's gas saturation always begins to decrease when the bulk equilibrium model's gas saturation has yet to reach its maximum. Since both models assume that the gas resides in the largest pore sizes, the calculation of the corresponding gas capillary pressure works the same. Thus, the three-phase bulk equilibrium model will have higher overall gas overpressures.

4.3.2 Minimum Methane Quantity Required To Fracture

We also investigate the seafloor depth's effect on fracture initiation. Since hydrates can form in offshore sediments with a range of seafloor depths, these different depths and pore pressures can change the conditions required for gas overpressure to initiate hydraulic fractures. We study this by running both of our phase saturation models with a given seafloor depth and zero methane quantity. We start increasing the methane quantity and solving for saturations and overpressures until the calculated overpressure

ratio becomes greater than unity, meeting our fracture criterion. Since the three-phase bulk equilibrium model calculates different gas overpressures than the three-phase stability model, we find that the two models require different methane quantities and corresponding gas saturations to initiate fractures for the same seafloor depth. We repeat this workflow for different seafloor depths. For these computations, we use Kumano Basin-like model parameters. Our reasoning is that the model parameters of Kumano Basin Site C0002 are not particularly considered as outliers; for instance, the pore size distribution is what we might expect for many other hydrate-bearing basins.

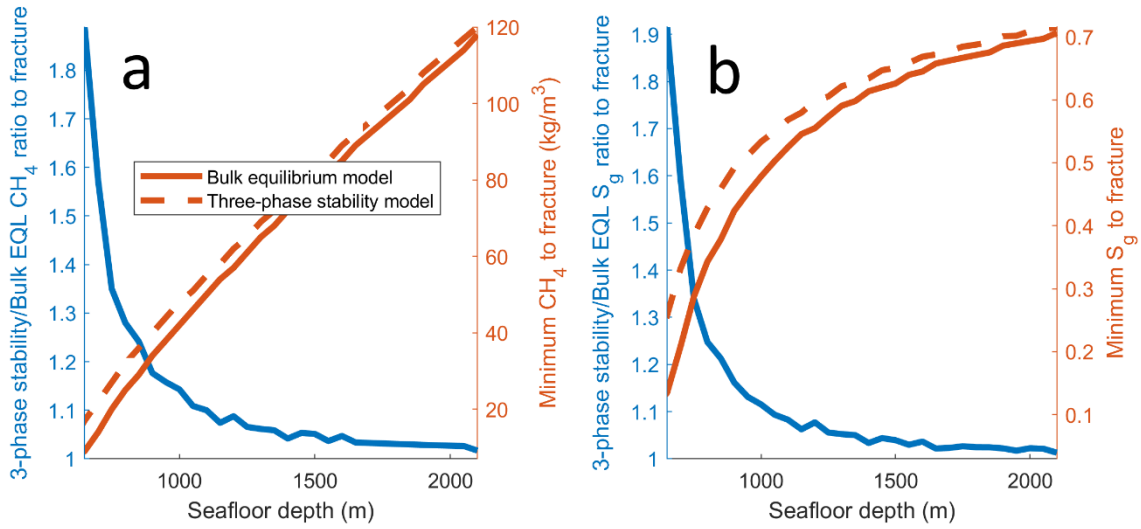

Figure 4.6 Results for seafloor depths from 600 to 2150 mbsl using Kumano Basin-like model parameters, showing a) the minimum methane quantity required to initiate a fracture for both overpressure models and b) the minimum gas saturation required to initiate a fracture for both overpressure models. On both figures, we also plot the ratio between the minimum methane quantities or minimum gas saturation, which we define as the value for the three-phase stability model divided by the three-phase bulk equilibrium model.

For all seafloor depths, we find that the three-phase bulk equilibrium model requires less methane quantity and less gas saturation than the three-phase stability model to initiate a hydraulic fracture. Thus, capillary effects inhibit the fracture initiation due to way the gas saturations decrease to zero towards the top of the three-phase zone. This causes the maximum overpressure in the three-phase stability model to usually occur at a deeper depth than the maximum for the three-phase bulk equilibrium model; the minimum horizontal effective stress at deeper depths are larger to overcome. The ratios of methane quantities and gas saturations between the two models show that this effect is much more significant for shallower seafloor depths, and this ratio appears to decay exponentially. Once the seafloor depth exceeds approximately 1200 meters, the difference between the two models' required fracture quantities becomes less than 10%.

For seafloor depths less than 650 mbsl, we encounter issues due to the calculated bulk methane solubilities. This is a limitation of our three-phase stability model since the capillary effects build off of the bulk solubility curves calculated using the chosen EOS. We find that the gas bulk solubility changes from decreasing with depth to increasing with depth. This begins to enlarge the three-phase stability zone to the point where the top of the three-phase zone is above the seafloor, and the gas phase is modeled to be present at extremely shallow depths.

For seafloor depths greater than 2150 mbsl, we find that the pore space becomes completely saturated with the hydrate phase, causing the minimum gas saturation to fracture to only reach 0.7 and not 1 for the seafloor depth of 2150 meters. For this situation, the hydrate phase completely saturates the pore space either above the depth of three-phase bulk equilibrium or above the top of the three-phase zone, depending on which model used. The maximum modeled gas saturation occurs either right below the depth of three-phase bulk equilibrium or at the bottom of the three-phase zone, and the

corresponding gas overpressure is not large enough to overcome the minimum horizontal effective stress to initiate a fracture. Therefore, capillary effects will not generate enough gas overpressure to initiate fractures for Kumano Basin-like sediments at seafloor depths greater than 2150 meters. Of course, the inclusion of realistic methane transport processes or other transient effects can change this depth limit.

Chapter 5: Bottom Simulating Reflections

In this chapter, we investigate the effect of the three-phase stability zone on the seismic response at the BSR, since the change in hydrate saturation and gas saturation within the three-phase zone causes a change in bulk density and compressional velocity. This should alter the BSR from a simple negative impedance contrast to a more complicated reflection. To investigate the varying seismic attributes of the BSR in response to a three-phase stability zone, we build our 1-D rock physics model of sediments at Blake Ridge, a location offshore South Carolina, USA, which was drilled by the Ocean Drilling Program (ODP) to characterize hydrate-bearing sediments (Paull and Matsumoto, 2000). Using this model, we generate synthetic seismograms and related plots in order to study the three-phase stability zone's effect.

With this rock physics model, we investigate the effect of the three-phase zone on the BSR by analyzing both the parameter sensitivity model and the original-resolution model. We perform a parameter sensitivity test by varying the phase saturation profiles within the three-phase zone and tracking how the rock and fluid properties change. For both models, we produce the resulting seismic responses at the BSR. Additionally, we run a variable methane quantity case for the original-resolution model based on the methane quantities reported by Dickens et al. (1997b).

5.1 DATA

Due to the availability of well log data, we perform our seismic analysis for Blake Ridge ODP Site 995. This section covers all the input data we use to build and run our rock physics model for the generation of synthetic seismograms.

5.1.1 ODP Site 995 Well Logs

As mentioned in section 3.2, we require many different rock and fluid properties to properly model the portion of the Blake Ridge formation that we are interested in. Since we are primarily interested in the background rock properties at the depths of and around the three-phase stability zone at Site 995, we show the well log data from 3200 meters below sea level (mbsl) to 3300 mbsl.

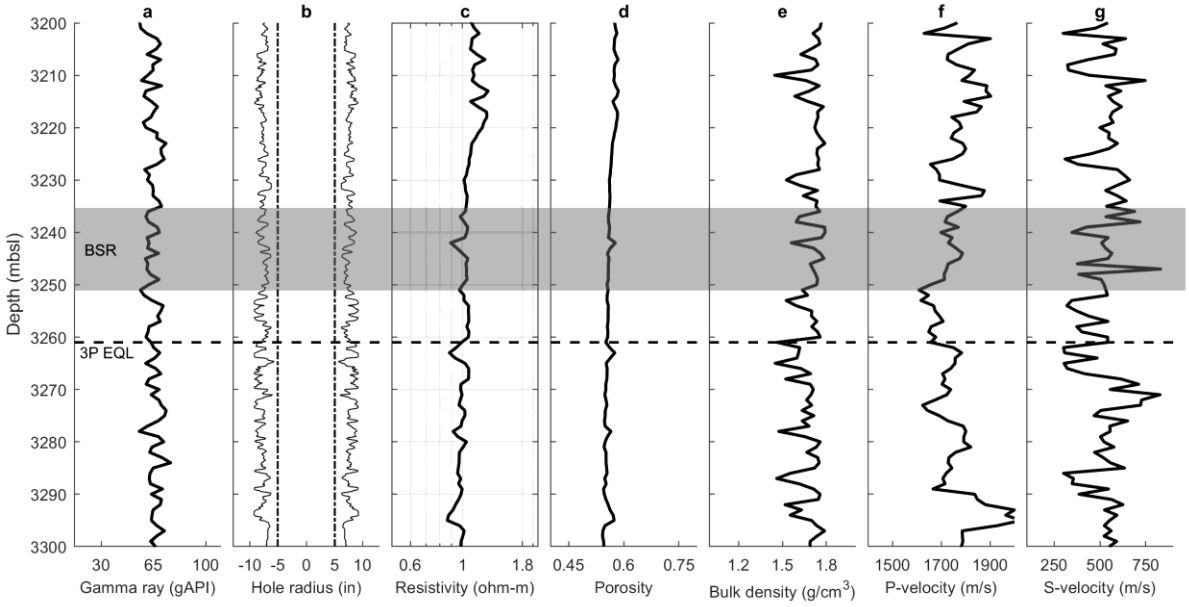

Figure 5.1 Background rock properties from ODP Site 995 well logs, showing the a) spectral gamma ray, b) caliper, c) resistivity, d) calculated porosity, e) bulk density, f) compressional wave velocity, and g) shear wave velocity. The shaded gray section indicates the BSR's estimated depth from 3236 mbsl to 3252 mbsl (Ruppel, 1997). The dashed horizontal line, marked as 3P EQL, indicates the depth of three-phase bulk equilibrium, where the hydrate-water bulk solubility is equal to the gas-water bulk solubility. At this depth, hydrate, gas, and water phases will be in equilibrium if we neglect capillary effects. In the caliper log, the dashed vertical lines represent the bit diameter, which indicates frequent caving over the entire logged interval (Guerin et al., 1999).

5.1.2 In-Situ Methane Quantity

Our rock physics model investigates methane quantities from 6 to 40 kg/m^3, with a different phase saturation profile attributed to each methane quantity. To run the variable methane quantity case, we use the methane quantities from Dickens et al. (1997b), which estimated in situ methane abundance at Site 995 using the Pressure Core Sampler (PCS) system. A continuous estimate of the methane quantity was developed in Dickens et al. (1997b), which interpolates through 17 PCS measurements taken over depths from approximately 2910 mbsl to 3370 mbsl. We use this profile to generate a more realistic phase saturation profile, which includes a three-phase transition zone spanning 3248 mbsl to 3272 mbsl.

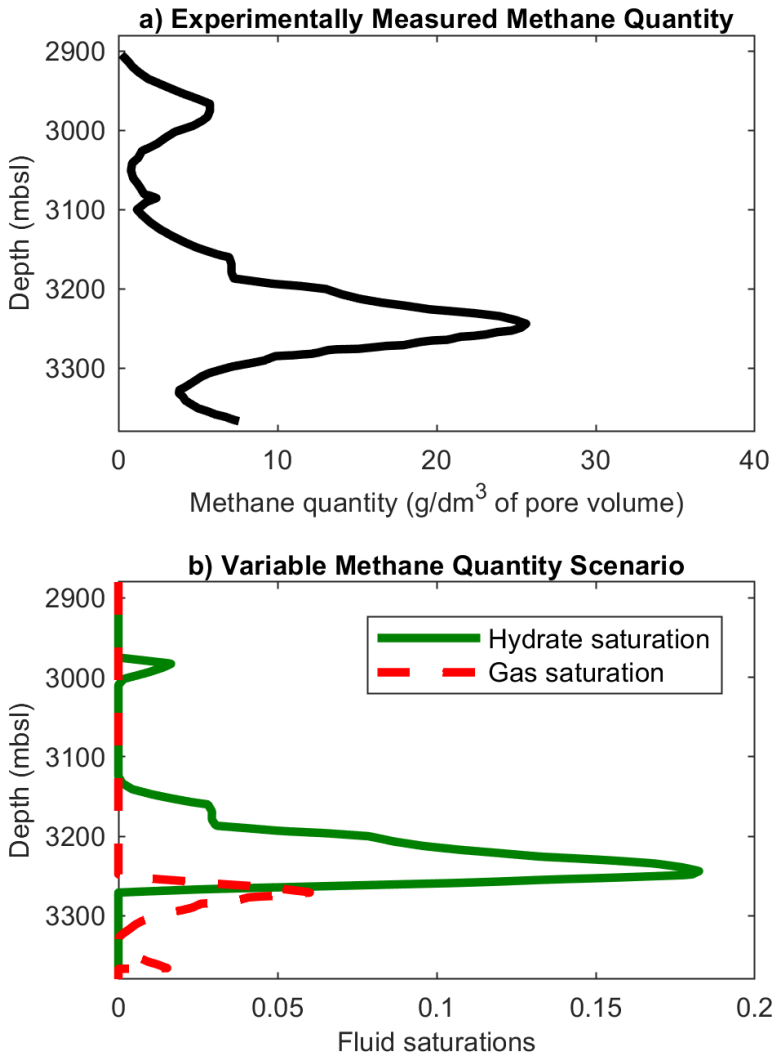

Figure 5.2 Experimental results from Blake Ridge Site 995 and Site 997 in Dickens et al. (1997b), showing a) methane quantity and b) calculated fluid saturations versus depth.

5.2 RESULTS

By combining the well log and MICP data, we can use our two rock physics models to calculate fluid substitution derived seismic properties of Site 995. We show some analysis of the seismic properties after fluid substitution for both models, and we

generate the synthetic seismograms over the BSR for different methane quantity cases. We also show how the two way travel time (TWTT) between the two positive peaks of the synthetic seismograms evolve as more methane is added into the system.

5.2.1 Parameter Sensitivity

Our parameter sensitivity study holds the background rock properties constant with depth while varying the fluid saturation profiles across the three-phase zone. The results of the fluid substitution calculations show how rock properties change with increasing methane quantity and three-phase zone thickness; in particular, we show how the bulk modulus, bulk density, shear wave velocity, and compressional wave velocity vary within the three-phase zone. In all of the sensitivity comparisons, baseline parameter values are established by running the model with no gas or hydrate content. As expected, the Gassmann/Hamilton model indicates that the fluid substituted bulk modulus decreases with increasing hydrate and gas saturation within and around the three-phase zone. The fluid substituted bulk density is directly affected by the changing fluid saturations because fluid density decreases as more methane is present in hydrate and gas phases. Since the shear modulus is held constant, the fluid substituted shear wave velocity increases slightly as the bulk density decreases. The resulting compressional wave velocity exhibits a large decrease across the three-phase zone, due to the drastic decrease in the bulk modulus when moving from hydrate-bearing sediments to gas-bearing sediments. The compressional wave velocity increases slightly in the upper hydrate layer as the hydrate saturation increases, due to a corresponding increase in the fluid bulk modulus. Since we assume the hydrate is pore-filling, this increase in compressional wave velocity is not very pronounced.

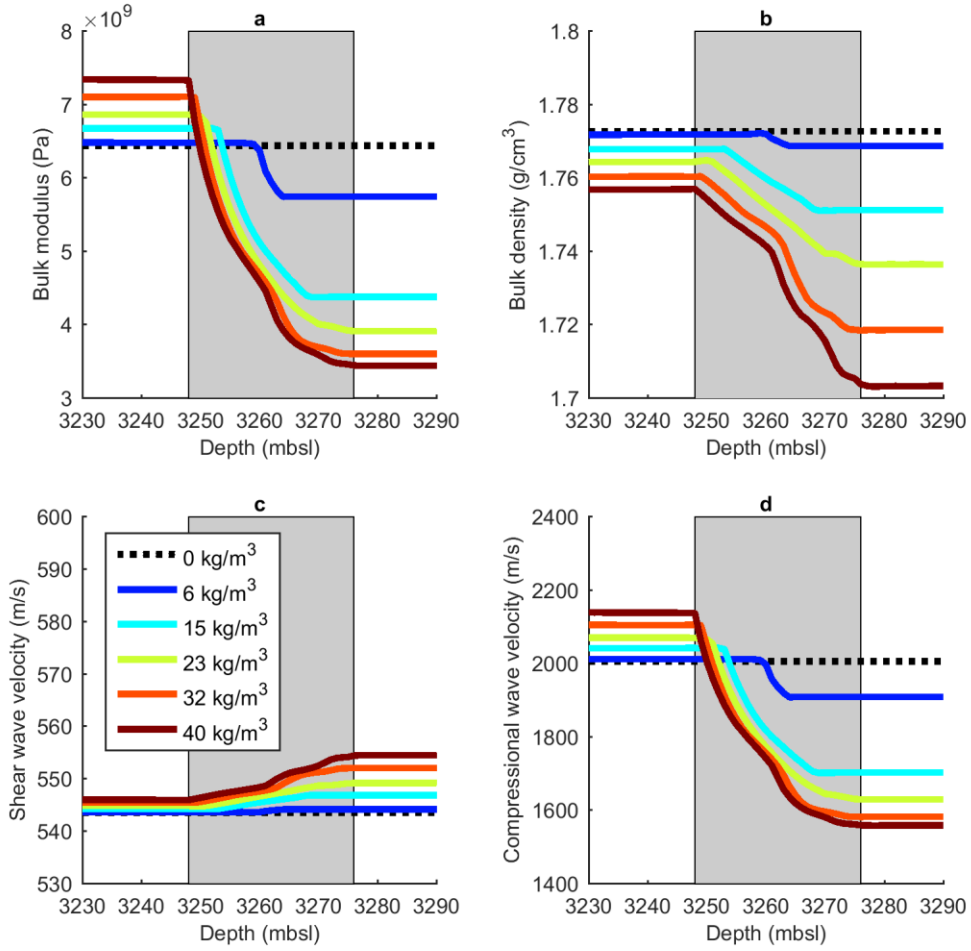

Figure 5.3 Parameter sensitivity results for a) bulk modulus, b) bulk density, c) shear wave velocity, and d) compressional wave velocity. The shaded gray region indicates the depths of the three-phase stability zone of the largest methane quantity case. The 0 kg/m^3 curves represent the base case where the rock physics model is fully water saturated. The parameter sensitivity analysis holds the rock properties constant across the entire depth in order to investigate the effect of different fluid saturation profiles.

5.2.2 Original Resolution Velocity Profiles

We also produce the compressional wave velocities corresponding to different methane quantities before upscaling the seismic properties of the upper hydrate layer and lower gas layer. In this case, the fluctuations in compressional velocity are driven by

variations in background rock properties. An important feature of the background velocity profile is the local minimum at 3263 mbsl. The location of this feature generally coincides with the middle of the three-phase zone, and the feature plays a large role in causing the steep velocity gradients within the depths of the three-phase zone. When comparing the base case velocity structure with the cases of varying methane quantity, we see that the varying methane quantity cases follow the same fluctuations seen in the base case's velocity structure. Local minima are located around the same depth, so the main difference is just the magnitude of the velocities. The wave velocities decrease in magnitude primarily because of the presence of gas saturation, and this effect increases as the methane quantity increases. However, the decrease in wave velocity due to gas saturation does not completely mask fluctuations of the background velocity profile, so we see an increase in wave velocity from the velocity minimum at 3263 mbsl to 3271 mbsl despite having higher gas saturation in this interval overall.

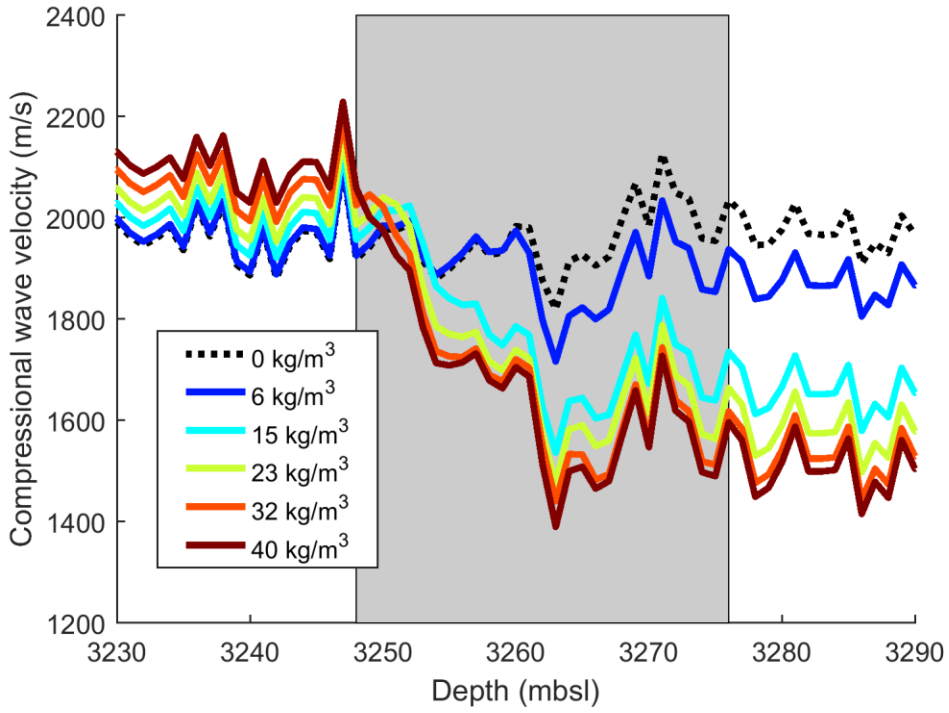

Figure 5.4 Velocity structure at the three-phase stability zone for the original-resolution model, showing a range of methane quantity cases. The shaded gray region indicates the depths of the three-phase stability zone of the largest methane quantity case. The base case of zero methane quantity is shown with the dashed line, which represents when the entire rock physics model is completely water saturated.

5.3 Discussion

5.3.1 Synthetic Seismograms

We generate seismograms across the BSR and BGHS using the parameter sensitivity model. As the methane quantity increases, the intersection of the maximum hydrate-water solubility and minimum gas-water solubility occurs at a shallower depth, elevating the depth of the BSR. The depth of the BSR, being the depth of the shallowest occurring gas saturation, ranges from 3260 mbsl for a methane quantity of 6 kg/m^3 to

3249 mbsl for a methane quantity of 40 kg/m^3. The impedance at the top of the three-phase zone decreases as more gas accumulates below because gas strongly decreases the compressional wave velocity. Similarly, the depth of the BGHS, being the deepest occurrence of hydrate saturation, becomes deeper as more methane is added to the formation, spanning 3263 mbsl at 6 kg/m^3 to 3276 mbsl at 40 kg/m^3. Thus, the thickness of the transition zone is 3 m at 6 kg/m^3, and the thickness increases until reaching a maximum of 27 m at a quantity of 40 kg/m^3.

The seismic response shows the reflection occurring at earlier TWTT as the methane quantity increases. This is due to the increase in the compressional velocity within the upper hydrate layer. Additionally, as the faster-velocity hydrate-bearing sediments transition to the slower-velocity gas-bearing sediments, the 30 Hz zero-phase Ricker wavelet undergoes a small phase rotation due to the decreasing compressional velocities through the three-phase zone. The wavelet resolution is close to 15 meters, so when the thickness of the three-phase zone becomes greater than the seismic resolution, the distance between the BSR and the BGHS becomes large enough for the reflection at the BGHS to be captured by the seismic wavelet and cause the phase rotation. The reflection's asymmetry is characterized by the leading peak amplitude being greater than the trailing peak amplitude.

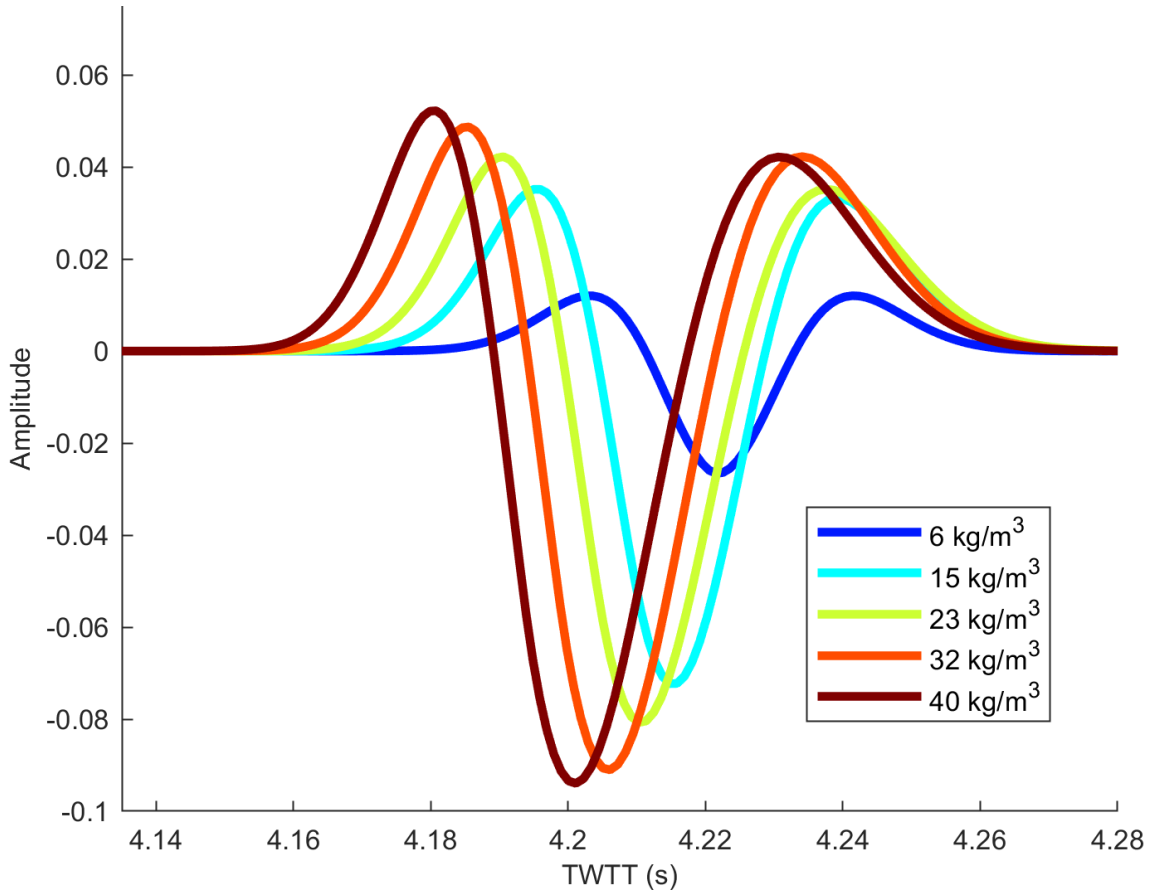

Figure 5.5 Synthetic seismograms in TWTT centered on the three-phase stability zone for the parameter sensitivity case. For each methane quantity case, the large negative polarity reflection represents the top of free gas, roughly representing the depth of the hypothetical BSR.

We also show the seismograms generated for the original-resolution model over the same range of methane quantities. The seismic response exhibits similar behavior to the parameter sensitivity results. Overall, the peak and trough amplitudes are increasing in magnitude when methane quantity increases. The reflected wavelet becomes out of phase for some methane quantities. The two way travel times decrease with more methane due to the increased hydrate saturation in the upper hydrate layer speeding up the compressional velocities. The asymmetry of the original-resolution seismograms is

reversed compared to the parameter sensitivity case seismograms; the leading peak amplitudes are smaller than the trailing peak amplitudes for all methane quantity cases. However, the trailing and leading peaks also seem to approach the same amplitude for a given methane quantity, as the methane quantity cases around 40 kg/m^3 show. By taking into account the results of the parameter sensitivity study, we believe that the reversed asymmetry of the original-resolution model is due to the fluctuations in the background rock properties.

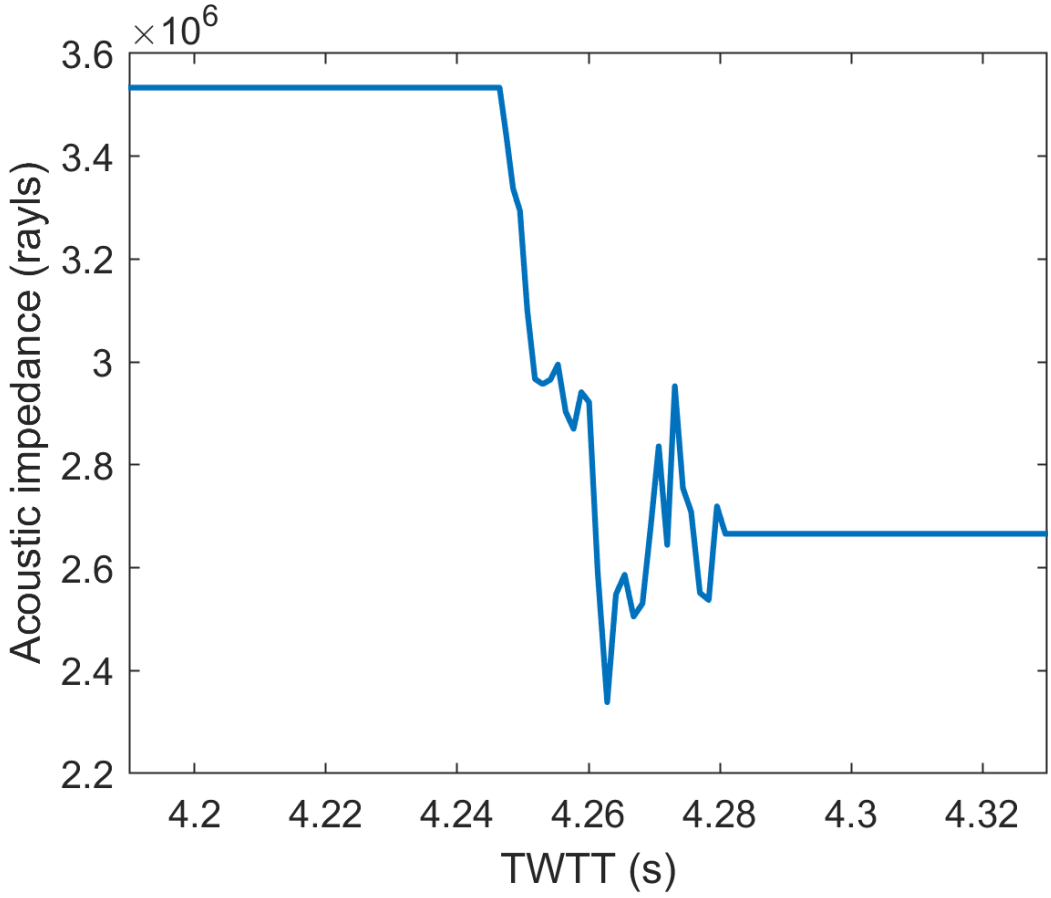

Figure 5.6 Acoustic impedance time series for the 40 kg/m^3 methane quantity case.

Specifically, the sharp velocity gradients, seen in the previous velocity profile figure, significantly affect the impedances and reflectances throughout the three-phase zone. All methane quantity cases exhibit positive reflectances for depths deeper than the local velocity minimum at 3263 mbsl, and these positive reflectances increase similar to how the velocity structure itself increases. These positive reflectances are what cause the seismograms' leading peak amplitude to be smaller than the trailing peak amplitude.

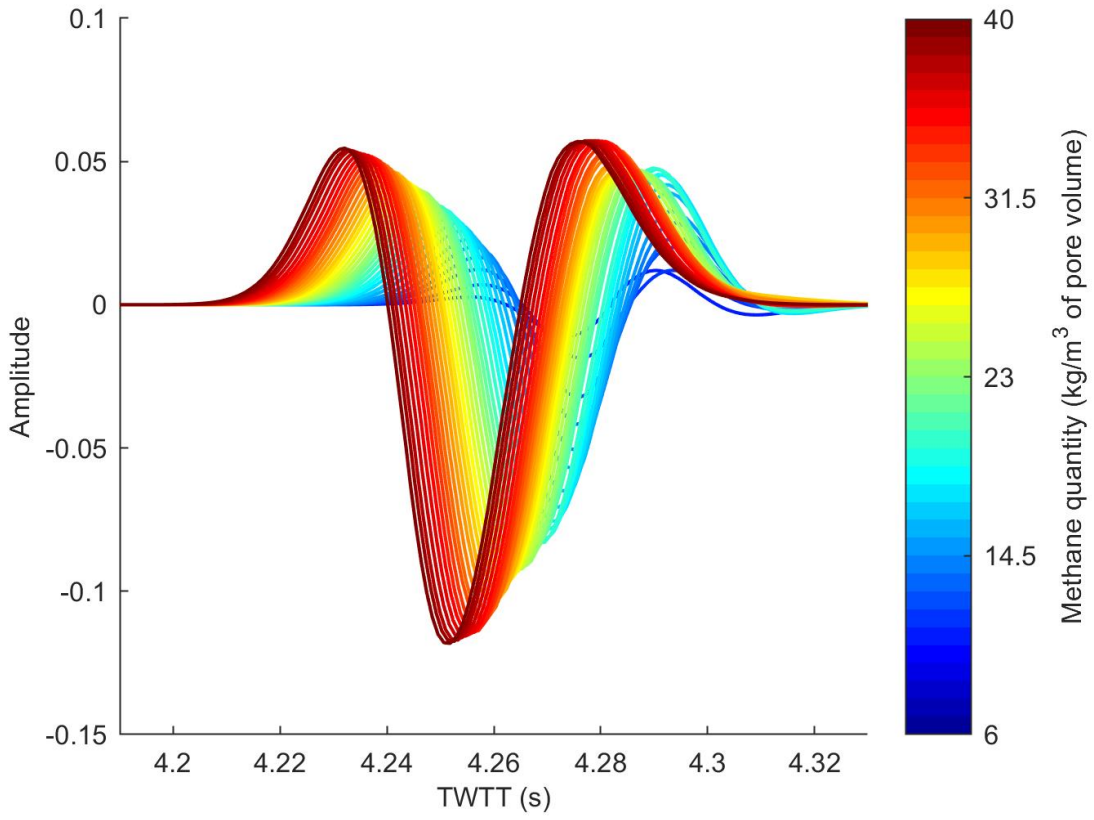

Figure 5.7 Synthetic seismograms in TWTT centered on the three-phase stability zone for the original-resolution model. The color bar shows successive seismograms of increasing methane quantity.

We next run our original-resolution rock physics model with the variable methane quantity scenario from section 5.1.2. Upon comparison, we see that the variable quantity case's leading peak TWTT and amplitude matches with the original-resolution model's constant 15 kg/m^3 case the closest. This is reasonable because 15 kg/m^3 corresponds well with the average methane quantity of the variable methane quantity case from 3200 mbsl to 3300 mbsl, which is our depths of interest in regards to the BSR and BGHS. At the same time, the methane quantity at the shallowest depth of gas lies near 15 kg/m^3, so it may be possible for the seismic reflection's leading positive peak amplitude to be an indicator of the methane quantity at the top of the three-phase zone. We also note that the variable quantity case's trailing peak amplitude is much larger than any amplitude seen in the entire range of constant methane quantity cases. This occurs because of the transition from a slow-velocity gas layer to a high-velocity water layer at 3350 mbsl. Since the gas saturation falls off to zero at 3350 mbsl, the upscaled gas layer below that depth is mostly water saturated. Therefore, the transition between the three-phase zone and the deeper, upscaled gas layer acts as a gas-water contact, which naturally induces a large positive reflectance. This positive reflectance produces the observed large amplitude peak at approximately a TWTT of 4.295 seconds. It is likely that the positive velocity gradients near the BGHS also magnify the large trailing peak amplitude.

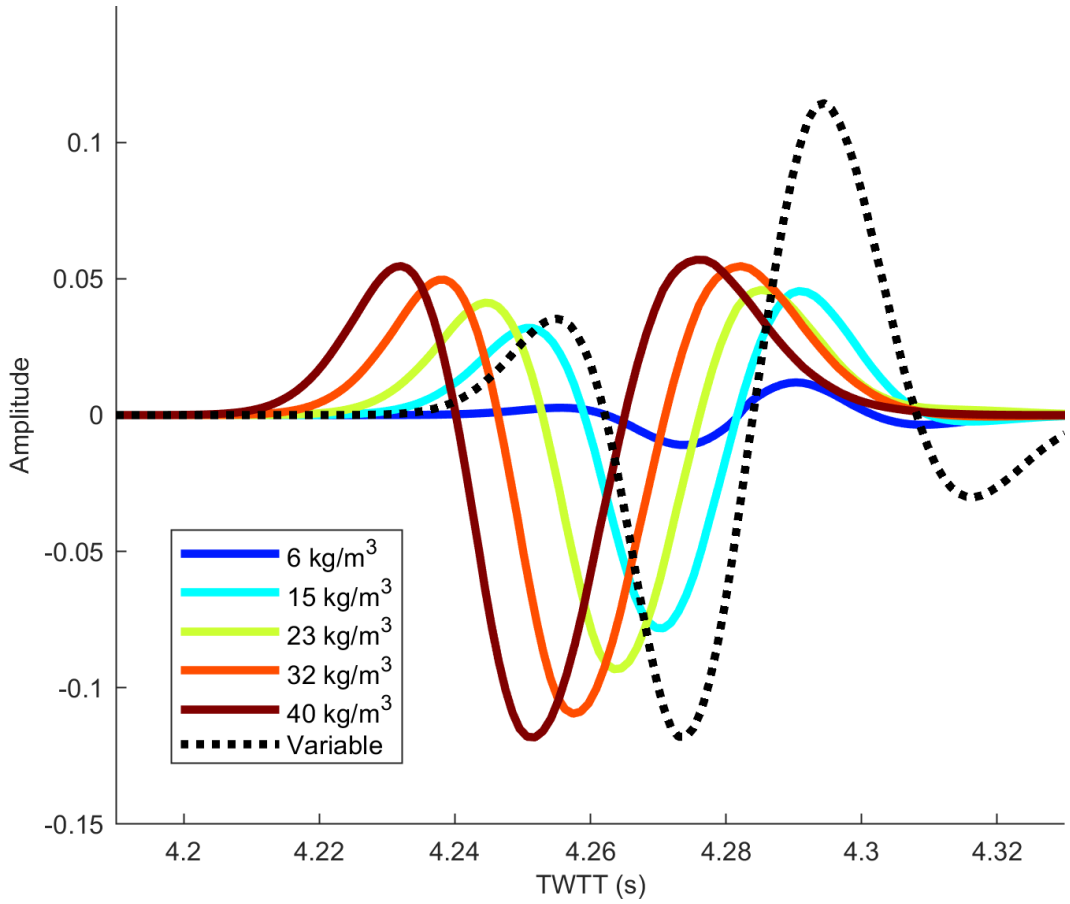

Figure 5.8 Synthetic seismogram in TWTT centered on the three-phase stability zone for the original-resolution model comparing a range of constant methane quantities against a variable methane quantity scenario.

5.3.2 Bottom Simulating Reflection Width

We analyze how the difference between the TWTT of the leading and trailing peak change as we add more methane to the system. The leading peak is taken to be the first positive peak near the BSR, and the trailing peak is taken to be the next positive peak. We define the difference between the peaks' TWTT as the TWTT of the trailing peak minus the TWTT of the leading peak so that the difference is positive. As we increase the methane quantity, the TWTT difference between the two peaks increases, due to the general enlargement of the three-phase zone thickness. The TWTT of the

leading peak decreases as more methane is added because the higher hydrate saturation in the upper hydrate layer increases the compressional velocity. This velocity increase also reduces the TWTT of the trailing peak; however, the gas saturation in the three-phase zone sharply drops the velocity, so the TWTT of the trailing peak decreases less than the TWTT of the leading peak. This velocity contrast above and below the BSR is what generates the TWTT difference between the two peaks.

The difference in TWTT trend appears to be a slightly nonlinear increase. The slope of the TWTT difference for lower methane quantities is greater than the slope at higher methane quantities. We believe that, at lower methane quantities and lower gas saturations, an incremental increase of gas saturation causes a greater velocity drop across the three-phase zone, which causes a large effect on the trailing peak's TWTT. However, at higher methane quantities and higher gas saturations, the velocity drop due to the incremental addition of gas saturation begins to plateau. This suggests that the velocity drop throughout the three-phase zone is mostly caused by the initial presence of gas, so subsequent gas additions at much higher gas saturations do not decrease the velocity enough to see continued widening of the peaks in TWTT.

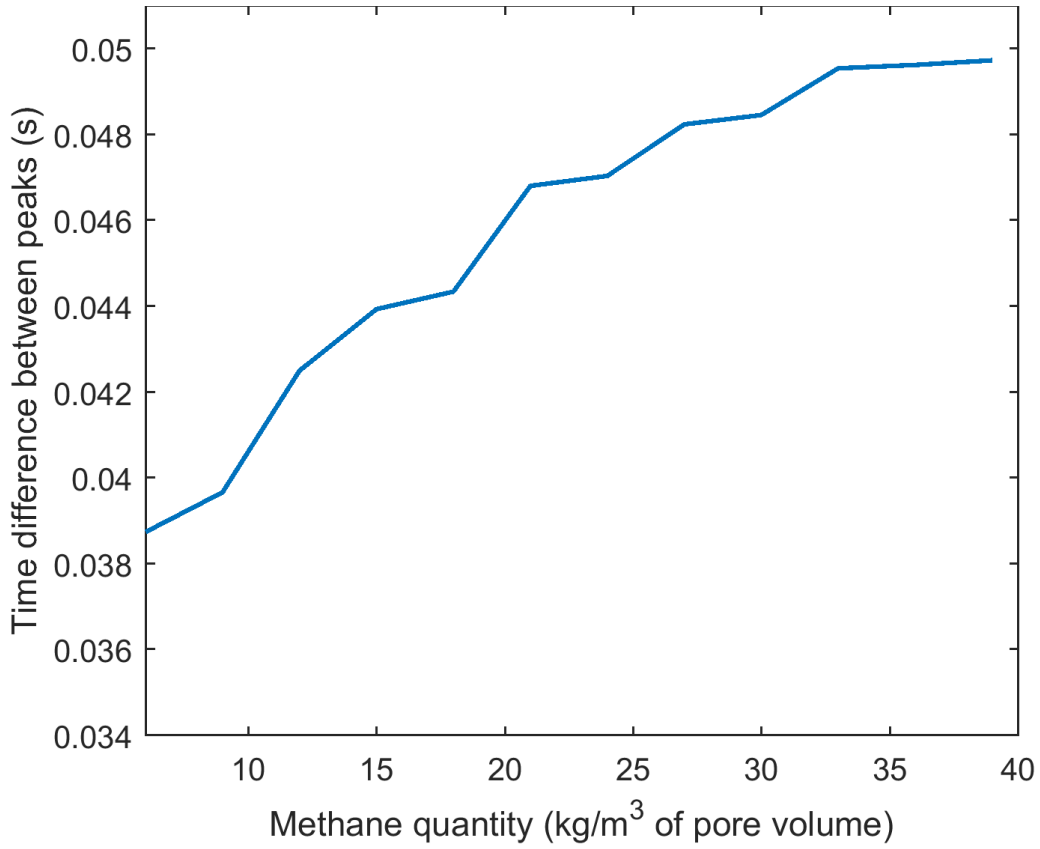

Figure 5.9 Difference in TWTT between the trailing and leading peaks of the BSR for the parameter sensitivity model.

We analyze the TWTT difference between the peaks of the seismic response generated over the original-resolution three-phase zone. Overall, the differences in TWTT are lower in magnitude compared to the differences seen from the parameter sensitivity model. Despite the heterogeneous effect of the background rock properties on the compressional wave velocities, the difference in TWTT between peaks generally increases as more methane is added to the system. However, the increasing trend appears even more nonlinear for the original-resolution model, making it difficult to determine what exactly is causing the slope changes in the TWTT difference behavior.

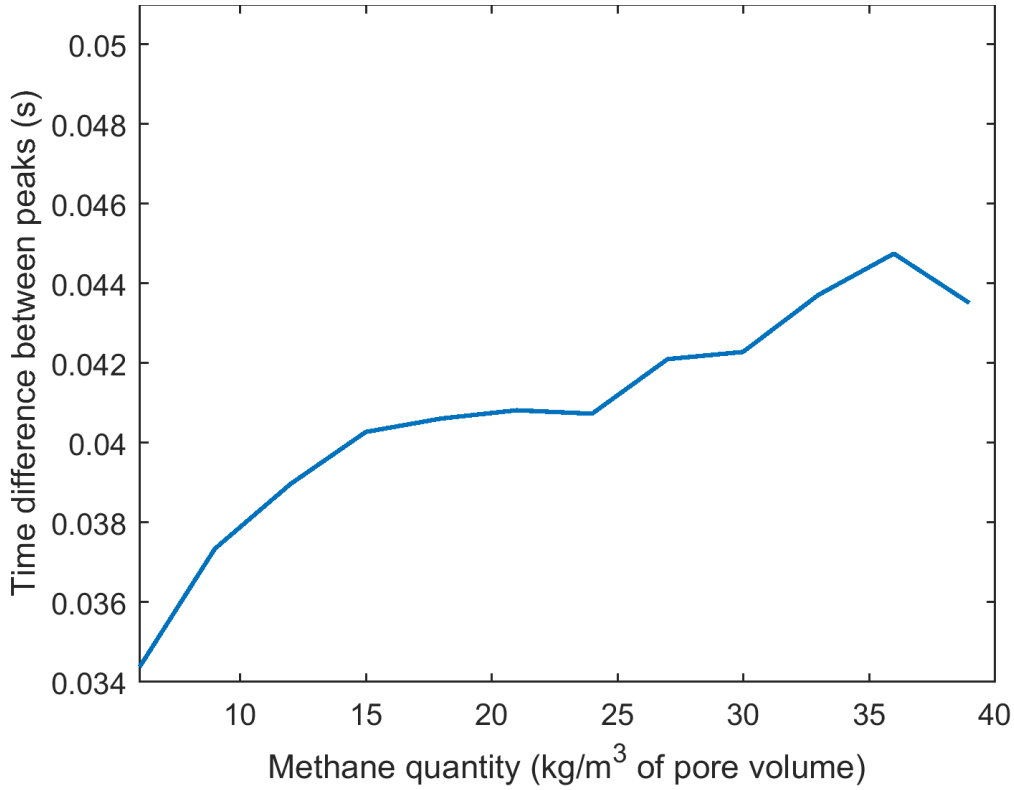

Figure 5.10 Difference in TWTT between the trailing and leading peak of the BSR for the original-resolution model. The y-axis limits are kept the same as the figure showing the difference in TWTT for the parameter sensitivity model for direct comparison.

Chapter 6: Conclusions and Future Work

In this work, we develop a three-phase stability model that implements capillary effects at static equilibrium conditions. By combining pressure and temperature conditions and mercury intrusion capillary pressure data, we can generate hydrate, gas, and water saturations within and around a three-phase stability zone. We advance the ideas behind three-phase stability by also minimizing the interfacial energy of our system by assuming that gas occupies the largest pores, water occupies the smallest pores, and hydrate occupies the pore sizes in between the two other phases.

We analyze two different applications of the three-phase stability zone throughout this work. The first application is the modeling of gas overpressures leading to the initiation of fractures. We compare the gas overpressures generated by the three-phase stability model against the gas overpressures generated by a three-phase bulk equilibrium model, which has a discrete base of hydrate stability because the capillary effects are neglected. For both phase saturation models, we also investigate the effect of different seafloor depths on the minimum amount of methane quantity required to initiate hydraulic fractures. The second application is the modeling of the seismic response of the three-phase stability zone. We use two 1-D rock physics models, the parameter sensitivity model and the original-resolution model, to study the seismic effects of three-phase stability through fluid substitution. We produce synthetic seismograms that vary depending on the methane quantity and the background rock properties. Finally, we conclude with the key points of our findings, and we present recommendations for future work.

6.1 KEY POINTS

1. In this work, we build on past three-phase stability models by integrating the theory of interfacial energy minimization. Our three-phase stability model can calculate hydrate, gas, and water saturations at static equilibrium as a function of pressure, temperature, and salinity, for a given pore size distribution and methane quantity.
2. When estimating the amount of methane required to initiate fractures due to gas overpressure, modeling with three-phase stability zones because of capillary effects will show that more methane is required than the amount shown when modeling without capillary effects. In other words, it is easier to initiate a fracture when assuming that there is a discrete base of hydrate stability. There are two main phenomena from capillary effects that comprise this result: elevated solubility within pores decreases gas saturation, and the bottom of the three-phase stability zone, where the gas saturation is at its maximum, commonly occurs beneath the depth of three-phase bulk equilibrium.
3. The inhibition of fracture initiation due to capillary effects is more significant for hydrate-bearing sediments with shallower seafloor depths. For seafloor depths around 650 mbsl, it can take up to twice the amount of methane to start a fracture, compared to the amount predicted by assuming a discrete base of hydrate stability. This result is relevant to how climate models that study the effect of methane emissions are affected by the seafloor venting of methane; shallower basins, which have shallower occurrences of gas phase buildup, are more likely to be characterized by active fracturing and methane venting through gas chimneys in response to temperature and pressure perturbations.

4. For hydrate-bearing sediments with very deep seafloors in static equilibrium, gas overpressure solely due to gas-water capillary pressure will not initiate fractures because the gas phase pressure will be smaller than the minimum horizontal stress.
5. Through parameter sensitivity analysis, we see that the three-phase stability zone causes a continuous decrease in compressional wave velocity, predominantly due to the gas saturation increasing from the top to the bottom of the three-phase zone.
6. The visible effect of the three-phase stability zone on the seismic response becomes prominent when the three-phase zone thickness becomes greater than the seismic wavelength resolution of approximately 15 m. For thicknesses greater than the seismic resolution, the negative velocity gradients due to the increase in gas saturation causes the seismic wave to undergo phase rotation. The behavior of the asymmetric peaks is influenced by the fluctuations in the background rock properties, and highly irregular heterogeneities can even counteract this effect, masking the phase rotation.
7. By analyzing the TWTT difference between the leading and trailing peaks across the width of the BSR, we find that an increase in methane quantity causes an increase in the TWTT difference for both the parameter sensitivity and the original-resolution model.
8. When varying the methane quantity in depth to achieve a more realistic model, we note the resulting seismic response can be approximated by matching with synthetic seismograms from constant methane quantity models. However, the underlying gas-water contact can cause a significantly larger trailing peak amplitude than what a constant methane quantity model will predict in the seismic response.

6.2 FUTURE RECOMMENDATIONS

1. When comparing the two gas overpressure models and identifying the minimum methane quantity to initiate a fracture, there are many more parameters than can be studied besides seafloor depth. Additional scenarios that should be tested include changing sea level height and changing seafloor temperature. This can study how climate change feedback mechanisms can play a role, since changing ocean conditions may induce fractures through gas overpressure; this may in turn cause more methane venting to the seafloor, complicating the climate change issue. A very interesting scenario than can take place in shorter timescales is a sediment landslide, where either sediment is added on top of the seafloor or altogether removed, causing quick changes in pressure, temperature, and rock stresses.
2. The integration of variable methane quantities over depth can improve the modeling of gas overpressures, since the variable methane quantities can generate more realistic phase saturation profiles. In the future, experimental PCS measurements may be taken from other hydrate-bearing basins, which can then be used in this work's modeling workflows to characterize the overpressures relative to the in situ rock stresses. On the other hand, it is possible that variable methane quantity models can be developed from existing well log datasets.
3. The fracture modeling and fracture criterion used in this work takes a simplified approach based on established literature. However, other fracturing models can be used to determine when a hydraulic fracture may initiate; for instance, geomechanics processes can be coupled with our workflow to improve the model by considering factors such as fracture toughness. Additionally, the more recent study of capillary fracturing may play a significant role in the future development

of this work's model. The analysis of how gas overpressure due to capillary pressure at the pore-scale may prove insightful to how other capillary-related effects influence the initiation of hydraulic fractures.

4. Further investigation into the conditions required for three-phase stability can be done. In particular, there may be condition that the calculated methane solubility for three-phase stability needs to be less than the maximum solubility for a hydrate-water system, not only less than the maximum solubility for a gas-water system. This builds on the theory of a global minimization of the system's methane solubility, whether it is for two-phase conditions or three-phase conditions.
5. The three-phase stability algorithm can be changed to use the system's methane solubility as an input to solve for the saturations and the methane quantity. For a given pressure, temperature, and methane solubility, the smallest pore size that hydrate or gas will occupy will be fixed. This is because the smallest pore size dictates the magnitude of the capillary pressure required to elevate the bulk methane solubility to the given methane solubility. Next, the interfacial energy minimization theory will partition the hydrate and gas saturations appropriately while meeting the capillary pressure requirements. Lastly, the mass balance on methane will simply calculate the methane quantity required to achieve this configuration. This alternative implementation may be used to generate methane quantity and three-phase saturation profiles for reservoir simulations if there are experimental measurements of methane solubility or concentration.
6. Quantitative analysis on the phase rotation of the seismic response at the BSR due to three-phase stability can be performed. The nature of the three-phase stability induced phase rotation is not well understood, and quantitative analysis can bring

more intuition to this phenomenon, even though large fluctuations in the background rock properties and the difficulty of sending zero-phase wavelets may make application of this analysis difficult. Preliminary work on investigating the ratio of the leading peak amplitude to the trailing peak amplitude has been done, but the results have been difficult to interpret. Further work can determine if the behavior of the peak amplitude ratio is a good indicator of model parameters like the methane quantity at the top of the three-phase zone. Another possible investigation may be to identify how the phase shift changes through Fourier analysis.

7. Amplitude versus offset (AVO) analysis can be used to investigate the effect of the three-phase stability zone. Preliminary work has been done to see how changing the horizontal offset of the seismic source and receiver affects the amplitude of the reflection over the BSR. There may be difficulty interpreting the results because AVO analysis is used to investigate a discrete boundary between two layers, instead of investigating the effect of a sediment layer itself. However, some insight may be gained from seeing how AVO crossplot samples change with increasing methane quantity.
8. While our work compares gas overpressure between a model that neglects capillary effects and a model that takes capillary effects into account, we do not do the same when investigating the seismic response over the BSR. Since we only generate synthetic seismograms for three-phase stability, we believe it would be good to compare these results to seismograms generated over a range of methane quantities assuming a discrete base of hydrate stability. As the methane quantity is increased, we expect these seismograms to shift to lower TWTT similar to the seismograms generated over three-phase stability zones. However, the

seismograms generated over a discrete boundary between hydrate and gas should show no phase rotation, and the TWTT difference between positive peaks should not increase with more methane.

9. Due to the simplicity of our static equilibrium three-phase stability model, our model can be easily integrated into transport and flow models. It is standard practice in reservoir simulation to assume local equilibrium within grid blocks. Thus, when adding transient processes like methane flux into our system, we should be able to use this work's algorithm to solve for three-phase saturations as long as the spatial and temporal discretization is fine enough to assume local equilibrium.

References

Anderson, R., Llamedo, M., Tohidi, B., & Burgass, R. W. (2003). Experimental measurement of methane and carbon dioxide clathrate hydrate equilibria in mesoporous silica. *The Journal of Physical Chemistry B*, *107*(15), 3507-3514. https://doi.org/10.1021/jp0263370

Anderson, R., Tohidi, B., & Webber, J. B. W. (2009). Gas hydrate growth and dissociation in narrow pore networks: capillary inhibition and hysteresis phenomena. *Geological Society, London, Special Publications*, *319*(1), 145-159. https://doi.org/10.1144/SP319.12

Archer, D., & Buffett, B. (2005). Time-dependent response of the global ocean clathrate reservoir to climatic and anthropogenic forcing. *Geochemistry, Geophysics, Geosystems*, *6*(3), Q03002. https://doi.org/10.1029/2004GC000854

Batzle, M., & Wang, Z. (1992). Seismic properties of pore fluids. *Geophysics*, *57*(11), 1396-1408.

Boswell, R. (2009). Is gas hydrate energy within reach?. *Science*, *325*(5943), 957-958. https://doi.org/10.1126/science.1175074

Brooks, R., & Corey, T. (1964). Hydraulic properties of porous media. *Hydrology Papers, Colorado State University*, *24*(3), 1-37. https://doi.org/10.13031/2013.40684

Bryan, G. M. (1974). In situ indications of gas hydrate. *Natural gases in marine sediments* (pp. 299-308). Boston, MA: Springer.

Collett, T. S. (1992). Potential of gas hydrates outlined. *Oil and Gas Journal, 90*(25), 84-87.

Collett, T. S., & Ladd, J. (2000). Detection of gas hydrate with downhole logs and assessment of gas hydrate concentrations (saturations) and gas volumes on the Blake Ridge with electrical resistivity log data. *Proceedings of the Ocean Drilling Program, Scientific Results*, *164*(1), 179-191. https://doi.org/10.2973/odp.proc.sr.164.219.2000

Clennell, M. B., Hovland, M., Booth, J. S., Henry, P., & Winters, W. J. (1999). Formation of natural gas hydrates in marine sediments: 1. Conceptual model of gas hydrate growth conditioned by host sediment properties. *Journal of Geophysical Research: Solid Earth*, *104*(B10), 22985-23003. https://doi.org/10.1029/1999JB900175

Dai, S., Santamarina, J. C., Waite, W. F., & Kneafsey, T. J. (2012). Hydrate morphology: Physical properties of sands with patchy hydrate saturation. *Journal of Geophysical Research: Solid Earth*, *117*(B11205). https://doi.org/10.1029/2012JB009667

Daigle, H., & Dugan B. (2011). Capillary controls on methane hydrate distribution and fracturing in advective systems. *Geochemistry, Geophysics, Geosystems*, *12*(1), Q01003. https://doi.org/10.1029/2010GC003392

Davie, M. K., Zatsepina, O. Y., & Buffett, B. A. (2004). Methane solubility in marine hydrate environments. *Marine Geology*, *203*(1-2), 177-184. https://doi.org/10.1016/S0025-3227(03)00331-1

Dickens, G. R., Castillo, M. M., & Walker, J. C. (1997a). A blast of gas in the latest Paleocene: Simulating first-order effects of massive dissociation of oceanic methane hydrate. *Geology*, *25*(3), 259-262. https://doi.org/10.1130/0091-7613(1997)025<0259:ABOGIT>2.3.CO;2

Dickens, G. R., Paull, C. K., & Wallace, P. (1997b). Direct measurement of in situ methane quantities in a large gas-hydrate reservoir. *Nature*, *385*(6615), 426. http://doi.org/10.1038/385426a0

Dillon, W. P., Danforth, W. W., Hutchinson, D. R., Drury, R. M., Taylor, M. H., & Booth, J. S. (1998). Evidence for faulting related to dissociation of gas hydrate and release of methane off the southeastern United States. *Geological Society, London, Special Publications*, *137*(1), 293-302. https://doi.org/10.1144/GSL.SP.1998.137.01.23

Duan, Z., Li, D., Chen, Y., & Sun, R. (2011). The influence of temperature, pressure, salinity and capillary force on the formation of methane hydrate. *Geoscience Frontiers*, *2*(2), 125-135. https://doi.org/10.1016/j.gsf.2011.03.009

Duan, Z., Møller, N., Greenberg, J., & Weare, J. H. (1992). The prediction of methane solubility in natural waters to high ionic strength from 0 to 250 C and from 0 to 1600 bar. *Geochimica et Cosmochimica Acta*, *56*(4), 1451-1460. https://doi.org/10.1016/0016-7037(92)90215-5

Dugan, B. (2015). Data report: porosity and pore size characteristics of sediments from Site C0002 of the Nankai Trough determined by mercury injection. *Proceedings of the Integrated Ocean Drilling Program*, *338*(1), 1-8. https://doi.org/10.2204/iodp.proc.338.202.2015

Dvorkin, J., Prasad, M., Sakai, A., & Lavoie, D. (1999). Elasticity of marine sediments: Rock physics modeling. *Geophysical Research Letters*, *26*(12), 1781-1784. https://doi.org/10.1029/1999GL900332

Ecker, C., Dvorkin, J., & Nur, A. (1998). Sediments with gas hydrates: Internal structure from seismic AVO. *Geophysics*, *63*(5), 1659-1669.

Erickson, S. N., & Jarrard, R. D. (1998). Porosity/formation-factor relationships for high-porosity siliciclastic sediments from Amazon Fan. *Geophysical Research Letters*, *25*(13), 2309-2312.

Expedition 314 Scientists (2009). Expedition 314 Site C0002. *Proceedings of the Integrated Ocean Drilling Program*, *314/315/316*(1), 1-77. https://doi.org/10.2204/iodp.proc.314315316.114.2009

Expedition 315 Scientists (2009), Expedition 315 Site C0002, *Proceedings of the Integrated Ocean Drilling Program*, *314/315/316*(1), 1–76, https://doi.org/10.2204/iodp.proc.314315316.124.2009

Flemings, P. B., Liu, X., & Winters, W. J. (2003). Critical pressure and multiphase flow in Blake Ridge gas hydrates. *Geology*, *31*(12), 1057–1060. https://doi.org/10.1130/G19863.1

Gassmann, F. (1951). Elastic waves through a packing of spheres. *Geophysics*, *16*(4), 673-685.

Guerin, G., Goldberg, D., & Meltser, A. (1999). Characterization of in situ elastic properties of gas hydrate-bearing sediments on the Blake Ridge. *Journal of Geophysical Research: Solid Earth*, *104*(B8), 17781-17795. https://doi.org/10.1029/1999JB900127

Hamilton, E. L. (1971). Elastic properties of marine sediments. *Journal of Geophysical Research*, *76*(2), 579–604. https://doi.org/10.1029/JB076i002p00579

Handa, Y. P., & Stupin, D. Y. (1992). Thermodynamic properties and dissociation characteristics of methane and propane hydrates in 70-Å-radius silica gel pores. *The Journal of Physical Chemistry*, *96*(21), 8599-8603. https://doi.org/10.1021/j100200a071

Helgerud, M. B., Waite, W. F., Kirby, S. H., & Nur, A. (2009). Elastic wave speeds and moduli in polycrystalline ice Ih, sI methane hydrate, and sII methane-ethane hydrate. *Journal of Geophysical Research: Solid Earth*, *114*(B02212). https://doi.org/10.1029/2008JB006132

Henry, P., Thomas, M., & Clennell, M. B. (1999). Formation of natural gas hydrates in marine sediments: 2. Thermodynamic calculations of stability conditions in porous sediments. *Journal of Geophysical Research: Solid Earth*, *104*(B10), 23005-23022. https://doi.org/10.1029/1999JB900167

Hillman, J. I. T., Cook, A. E., Sawyer, D. E., Küçük, H. M., & Goldberg, D. S. (2017). The character and amplitude of 'discontinuous' bottom-simulating reflections in marine seismic data. *Earth and Planetary Science Letters*, *459*, 157-169. https://doi.org/10.1016/j.epsl.2016.10.058

Hornbach, M. J., Saffer, D. M., & Holbrook, W. S. (2004). Critically pressured free-gas reservoirs below gas-hydrate provinces. *Nature*, *427*(6970), 142–144. https://doi.org/10.1038/nature02172

Jain, A. K., & Juanes, R. (2009). Preferential Mode of gas invasion in sediments: Grain-scale mechanistic model of coupled multiphase fluid flow and sediment

mechanics. *Journal of Geophysical Research: Solid Earth*, *114*(B8), B08101. https://doi.org/10.1029/2008JB006002

Karig, D. E., & Hou, G. (1992). High-stress consolidation experiments and their geologic implications. *Journal of Geophysical Research: Solid Earth*, *97*(B1), 289-300. https://doi.org/10.1029/91JB02247

Kraemer, L. M., Owen, R. M., & Dickens, G. R. (2000). Lithology of the upper gas hydrate zone, Blake Outer Ridge: a link between diatoms, porosity, and gas hydrate. *Proceedings of the Ocean Drilling Program, Scientific Results*, *164*(1), 229-236. https://doi.org/10.2973/odp.proc.sr.164.221.2000

Kvenvolden, K. A. (1993). Gas hydrates—geological perspective and global change. *Reviews of Geophysics, 31*(2), 173–187 https://doi.org/10.1029/93RG00268

Kvenvolden, K. A., & Barnard, L. A. (1983). Hydrates of natural gas in continental margins. *Studies in Continental Margin Geology*, *34*, 631-640.

Lee, M. W., Hutchinson, D. R., Collett, T. S., & Dillon, W. P. (1996). Seismic velocities for hydrate-bearing sediments using weighted equation. *Journal of Geophysical Research: Solid Earth*, *101*(B9), 20347-20358. https://doi.org/10.1029/96JB01886

Leverett, M. C. (1941). Capillary behavior in porous solids. *Transactions of the AIME*, *142*(1), 152–169. https://doi.org/10.2118/941152-G

Liu, X., & Flemings, P. B. (2006). Passing gas through the hydrate stability zone at southern Hydrate Ridge, offshore Oregon. *Earth and Planetary Science Letters*, *241*(1-2), 211-226. http://doi.org/10.1016/j.epsl.2005.10.026

Liu, X., & Flemings, P. B. (2011). Capillary effects on hydrate stability in marine sediments. *Journal of Geophysical Research*, *116*(7), B07102. http://doi.org/10.1029/2010JB008143

Mavko, G., Mukerji, T., & Dvorkin, J. (2009). *The rock physics handbook: Tools for seismic analysis of porous media*. Cambridge, UK: Cambridge University Press.

Miyakawa, A., Saito, S., Yamada, Y., Tomaru, H., Kinoshita, M., & Tsuji, T. (2014). Gas hydrate saturation at Site C0002, IODP Expeditions 314 and 315, in the Kumano Basin, Nankai trough. *Island Arc*, *23*(2), 142-156. http://doi.org/10.1111/iar.12064

Østergaard, K. K., Anderson, R., Llamedo, M., & Tohidi, B. (2002). Hydrate phase equilibria in porous media: effect of pore size and salinity. *Terra Nova*, *14*(5), 307-312. https://doi.org/10.1046/j.1365-3121.2002.00433.x

Pabst, W., & Gregorová, E. (2013). Elastic properties of silica polymorphs—a review. *Ceramics-Silikáty*, *57*(3), 167-184.

Paull, C. K., et al. (1996). Gas hydrate sampling on the Blake Ridge and Carolina Rise. *Proceedings of the Ocean Drilling Program, Scientific Results*, 164.

Paull, C. K., & Matsumoto, R. (2000). Leg 164 overview. *Proceedings of the Ocean Drilling Program, Scientific Results*, *164*, 3-10.

Pearson, C. F., Halleck, P. M., McGuire, P. L., Hermes, R., & Mathews, M. (1983). Natural gas hydrate deposits: A review of in situ properties. *The Journal of Physical Chemistry*, *87*(21), 4180-4185.

Reynolds, J. M. (1997). *An introduction to applied and environmental geophysics* (pp. 796). Chichester, UK: John Wiley & Sons.

Ruppel, C. (1997). Anomalously cold temperatures observed at the base of the gas hydrate stability zone on the U.S. Atlantic passive margin. *Geology*, *25*(8), 699-702. https://doi.org/10.1130/0091-7613(1997)025<0699:ACTOAT>2.3.CO;2

Schlumberger Limited. (2000). *Log Interpretation Charts*. Sugar Land, TX: Schlumberger Limited.

Shipboard Scientific Party. (1996) Site 995. *Proceedings of the Ocean Drilling Program, Initial Reports*, *164*, 175–240.

Shipley, T. H., Houston, M. H., Buffler, R. T., Shaub, F. J., McMillen, K. J., Ladd, J. W., & Worzel, J. L. (1979). Seismic evidence for widespread possible gas hydrate horizons on continental slopes and rises. *AAPG bulletin*, *63*(12), 2204-2213. https://doi.org/10.1306/2f91890a-16ce-11d7-8645000102c1865d

Smith, D. H., Wilder, J. W., & Seshadri, K. (2002). Methane hydrate equilibria in silica gels with broad pore-size distributions. *AIChE Journal*, *48*(2), 393-400. https://doi.org/10.1002/aic.690480222

Sun, R., & Duan, Z. (2007). An accurate model to predict the thermodynamic stability of methane hydrate and methane solubility in marine environments. *Chemical Geology*, *244*(1-2), 248-262. https://doi.org/10.1016/j.chemgeo.2007.06.021

Tréhu, A. M., Long, P. E., Torres, M. E., Bohrmann, G., Rack, F. R., Collett, T. S., et al. (2004). Three-dimensional distribution of gas hydrate beneath southern Hydrate Ridge: constraints from ODP Leg 204. *Earth and Planetary Science Letters*, *222*(3-4), 845-862. http://doi.org/10.1016/j.epsl.2004.03.035

Tréhu, A. M. (2006). Subsurface temperatures beneath southern Hydrate Ridge. *Proceedings of the Ocean Drilling Program, Scientific Results*, *204*(1), 1-26. https://doi.org/10.2973/odp.proc.sr.204.114.2006

Tucholke, B. E., Bryan, G. M., & Ewing, J. I. (1977). Gas-hydrate horizons detected in seismic-profiler data from the western North Atlantic. *AAPG bulletin*, *61*(5), 698-707. https://doi.org/10.1306/C1EA3DC5-16C9-11D7-8645000102C1865D

Uchida, T., Ebinuma, T., & Ishizaki, T. (1999). Dissociation condition measurements of methane hydrate in confined small pores of porous glass. *The Journal of Physical Chemistry B*, *103*(18), 3659-3662. https://doi.org/10.1021/jp984559l

Uchida, T., Takeya, S., Chuvilin, E. M., Ohmura, R., Nagao, J., Yakushev V.S., et al. (2004). Decomposition of methane hydrates in sand, sandstone, clays, and glass beads. *Journal of Geophysical Research: Solid Earth*, *109*(B05206). https://doi.org/10.1029/2003JB002771

Valko, P., & Economides, M. J. (1995). *Hydraulic fracture mechanics* (pp. 298). Chichester, England: John Wiley & Sons.

Van Genuchten, M. T. (1980). A closed-form equation for predicting the hydraulic conductivity of unsaturated soils. *Soil Science Society of America Journal*, *44*(5), 892-898. https://doi.org/10.2136/sssaj1980.03615995004400050002x

Waite, W. F., Santamarina, J. C., Cortes, D. D., Dugan, B., Espinoza, D. N., Germaine, J., et al. (2009). Physical properties of hydrate-bearing sediments. *Reviews of Geophysics*, *47*(RG4003), 1–38. https://doi.org/10.1029/2008RG000279